Chemical Engineering Journal 483 (2024) 149429

Contents lists available at ScienceDirect

Chemical Engineering Journal

journal homepage: www.elsevier.com/locate/cej

Mechanistic insights into silver-gold nanoalloy formation by two-dimensional population balance modeling

N.E. Traoré [a,b], T. Schikarski [a,b], A. Körner [c], P. Cardenas Lopez [a,b], L. Hartmann [a,b], B. Fritsch [c], J. Walter [a,b], A. Hutzler [c], L. Pflug [d,e,*], W. Peukert [a,b,*]

[a] Institute of Particle Technology, Friedrich-Alexander-Universität Erlangen-Nürnberg, Cauerstraße 4, 91058 Erlangen, Germany
[b] Interdisciplinary Center for Functional Particle Systems, Friedrich-Alexander-Universität Erlangen-Nürnberg, Haberstraße 9a, 91058 Erlangen, Germany
[c] Helmholtz Institute Erlangen-Nürnberg for Renewable Energy (IEK-11), Forschungszentrum Jülich GmbH, Cauerstraße 1, 91058 Erlangen, Germany
[d] Chair of Applied Mathematics (Continuous Optimization), Friedrich-Alexander-Universität Erlangen-Nürnberg, Cauerstraße 11, 91058 Erlangen, Germany
[e] FAU Competence Center Scientific Computing, Friedrich-Alexander-Universität Erlangen-Nürnberg, Martensstr. 5a, 91058 Erlangen, Germany

ARTICLE INFO

Keywords:
Population Balance Equation
Nanoparticle Synthesis
Formation Mechanism
Silver Nanoparticle
Gold Nanoparticle
Alloy Nanoparticle

ABSTRACT

The large-scale synthesis of nanoparticles (NPs) with defined properties requires detailed understanding of the underlying formation mechanisms and kinetics. The formation mechanisms of bimetallic NPs are still not sufficiently understood due to the complex reaction chemistry, which makes the control of the supersaturation as the thermodynamic driving force challenging. Particle size, chemical composition, and the distribution of the elements within the particles change dynamically during particle formation. In this work, we propose a mechanism for the formation of bimetallic silver-gold alloy NPs via a green liquid-phase co-reduction synthesis and develop a two-dimensional population balance model to quantitatively describe the evolution of particle size distribution, composition, and optical properties. We shed light on the complex multi-stage formation mechanism of a highly relevant bimetallic NP system, lay the foundation for tailoring the process conditions to achieve targeted optical particle properties and unravel predictive property-process relationships.

1. Introduction

Plasmonic nanoparticles (NPs) have received increasing attention in recent years due to their unique properties, which are mainly determined by the NPs' size, material, and spatial material distribution. Plasmonic NPs are characterized by their localized surface plasmon resonance (LSPR) induced by their interaction with the electromagnetic field of the incident light and are widely applied, for instance in plasmonic sensors [1,2], in catalytic applications [3] and in medicine as contrast agents for computed tomography [4–6]. For commercial applications, scale-up from the lab to production scale requires detailed understanding and control over the formation mechanisms and kinetics. The precise tuning of the supersaturation profile as the thermodynamic driving force within the reactor directly affects the resulting particle size distribution (PSD) of the produced particles [7]. In general, the supersaturation is key for knowledge-based property and process design based on adequate models for the formation dynamics, effectively spanning the property-process function of the respective system.

For monometallic NPs a range of formation mechanisms for a variety of synthesis routes have been proposed in literature. In particular, Polte *et al.* investigated the formation mechanism of silver and gold NPs in detail. They studied the chemical reduction of silver and gold precursors with sodium borohydride [8,9] and sodium citrate [10,11] by means of *in situ* XANES and SAXS measurements. Further, Wu *et al.* proposed a mechanism for a green synthesis of gold NPs [12] and Harada *et al.* for a polymer-based photoreduction synthesis of gold NPs [13].

Plasmonic silver-gold alloy NPs (ANPs) are highly relevant because silver and gold are the two elements with the strongest LSPR [14] and their alloys offer additional degrees of freedom for the design of optical properties [15]. Alloys of these materials show unique optical properties in dependence of their size, shape, and composition [16–18]. These particles find applications in catalysis [19], as antibacterial agents [20] or as a model system to better understand the formation of bimetallic NPs due to their almost identical lattice constants [21–23]. Several synthesis pathways are discussed in literature [17,24,25].

Only very few attempts exist to describe the underlying formation mechanisms. One example is a study by Nguyen *et al.*, who described the formation of homogeneous silver-gold alloy NPs via a laser induced co-

* Corresponding authors at: Martenstr. 5a, 91058 Erlangen, Germany (L. Pflug), Cauerstr. 4, 91058 Erlangen (W. Peukert)
E-mail addresses: lukas.pflug@fau.de (L. Pflug), wolfgang.peukert@fau.de (W. Peukert).

https://doi.org/10.1016/j.cej.2024.149429
Received 13 December 2023; Received in revised form 24 January 2024; Accepted 5 February 2024
Available online 6 February 2024

reduction process. Based on *in situ* extinction measurements, the extracted LSPR positions and the extinction values at the LSPR position, they propose the formation of gold-rich nuclei, which over time grow to alloy NPs with the respective desired composition. They extract effective formation kinetics from the extinction values over time. However, model-based simulations were not performed to support their findings [26]. Garcia *et al.* observed the size evolution of silver-gold alloy NPs via *in situ* SAXS measurements. They conclude the growth of a single size species with two distinct growth rate regimes with faster growth in the beginning and a slower one towards the end of the reaction. No information of the evolution of composition or elemental distribution within the particles over time is available and no formation mechanism is proposed [27]. Blommaerts *et al.* investigated the formation of AgAu ANPs via the Turkevich method and described the different reduction rates of gold and silver ions and the change in the elemental distribution of gold and silver over the particle diameter over time. They described several steps in the formation of the particles [28].

Many publications focus on the formation of pure noble metal NPs. In contrast, we study the formation mechanism of AgAu alloy NPs and propose a population balance model for their formation dynamics. During particle formation, particle size, chemical composition, and the spatial distribution of Au and Ag over the particle diameter change dynamically. The formation mechanism of silver-gold alloy NPs produced via the chemical co-reduction method is not sufficiently understood, and, to the best of our knowledge, no predictive model has been developed.

The formation of bimetallic NPs, especially via liquid phase co-reduction methods, depends on several nonlinearly coupled chemical elementary processes. This is mainly because not only the supersaturation of one but of both metal precursors needs to be controlled simultaneously. If process conditions like pH, temperature or concentration ratios are varied, the changes typically affect the reactions of both metal precursors differently, leading to changes in composition and particle size. For silver-gold ANPs a particular challenge is the precipitation of solid AgCl from reaction mixtures containing silver ions (from the silver precursor) and chloride ions (from the gold precursor) [19,25]. This leads to a decrease in the concentration of silver in solution and thus strongly influences the incorporation of silver into the alloy. Therefore, syntheses of silver-gold ANPs at room temperature are usually limited to metal precursor concentrations below the (very low) solubility of AgCl in water, which leads to extremely diluted dispersions, limiting the transfer to large-scale applications.

We recently demonstrated a green, reaction-controlled synthesis route for silver-gold ANPs at room temperature, which, in contrast to most other room-temperature syntheses, works at remarkably high metal precursor concentrations [16]. This reaction-controlled synthesis runs for 17 to 24 h, is readily scalable, and produces narrowly distributed particles around 7 nm with all compositions between pure Au and Ag. Due to the slow reaction rates, it is predestined for an in-depth analysis of the formation mechanism over time.

In this paper we therefore aim to describe the formation mechanism of an aqueous co-reduction synthesis of homogeneous silver-gold alloy NPs. Based on the understanding of the formation mechanism we develop a predictive two-dimensional population balance model for their formation. Quantitative comparison of the simulated and experimentally determined final PSD and of resulting optical properties over the course of the reaction shed light on the complex formation pathway. Such models are not limited to the synthesis of bimetallic ANPs but are based on a widely applicable general approach [29]. In principle, nanoparticle formation follows a sequence of mixing, reaction, nucleation and growth. Examples include the reaction-controlled synthesis of quantum dots [30] and even the mixing-controlled formation of organic particles like ibuprofen [31]. In this study we investigate a reaction controlled process, where mixing is much faster than the reaction kinetics. It paves the way for process design to achieve desired optical particle properties and to develop predictive property-process relationships for plasmonic NPs.

2. Materials and methods

2.1. Synthesis of silver-gold alloy nanoparticles

All reagents have been used without further purification. Hydrogen tetrachloroaurate(III) trihydrate was purchased from Sigma Aldrich, aqueous silver nitrate solution (1 M) from VWR Chemicals, dextran with a molecular weight of 40 kDa from ITW Reagents, and an aqueous sodium hydroxide solution (1 M) from Honeywell. Deionized water (>17 MΩ cm) was used for all experiments.

Silver-gold alloy NPs with varying molar gold contents were synthesized based on a priorly published synthesis protocol [16]. In short, 5 g of dextran were dissolved in 100 mL of deionized water. From this solution, 4.5 mL were transferred to a 10 mL snap cap vial and mixed with x mL of $HAuCl_4$ (1 mM) and (1-x) mL of $AgNO_3$ (1 mM). By varying x between 0 and 1 the molar gold content of the resulting particles was tuned. After mixing, 0.5 mL of NaOH (10 mM) was added and the solution mixed again and stored under dark conditions. After around 48 h, stabilized nanoalloy particles with defined molar gold content were formed. For in-line UV–Vis measurements, the synthesis was conducted in a cuvette within the spectrometer.

2.2. Methods

2.2.1. UV–Vis spectroscopy

A Varian Cary 100 spectrophotometer with a wavelength range of 200 nm to 800 nm per spectrum and a spectral resolution of 1 nm was used for all UV–Vis spectroscopy measurements, both in-line and off-line. All samples were measured against a reference of pure water without any further dilution or purification. Single-use plastic UV–Vis cuvettes with an optical path length of 1 cm were used for all experiments.

2.2.2. Analytical ultracentrifugation (AUC)

The PSDs of the ANPs were determined in the liquid phase via sedimentation velocity analytical ultracentrifugation (SV-AUC) experiments. The data was collected via a commercial type Optima AUC, from Beckmann Coulter. The samples were measured without further purification or dilution in both titanium centerpieces from Nanolytics Instruments and 3D printed centerpieces [32] with an optical path length of 12 mm. All experiments were carried out at 20 °C after temperature equilibration for at least 5 h. Sedimentation data was acquired with at least 450 scans, a radial step of 50 μm, a rotor revolution of 15 000 rpm, and a detection wavelength of 300 nm. In the case of glutathione (GSH) stabilized Ag NPs, the rotor speed was 25 000 rpm and the detection wavelength was 450 nm.

The obtained sedimentation data was analyzed with the ls-g*(s) model in the software Sedfit (version 16-1c). [33] The data was fitted with a resolution of 150 grid points for the sedimentation coefficient. It was corrected for time and radial invariant noise during the analysis and a second derivative regularization with a confidence level of 0.90 was applied to mitigate fluctuations in the retrieved distributions.

2.2.3. Scanning transmission electron microscopy (STEM) and energy-dispersive X-ray spectroscopy (EDXS)

High-angle annular dark field scanning transmission electron microscopy (HAADF-STEM) was performed using a Thermo Fisher Scientific Talos F200i with a Schottky field-emission gun (X-FEG) at an acceleration voltage of 200 kV, a beam current of 32 pA, and a convergence angle of 10.5 mrad. A high-angle annular dark field

detector covering an angular range of 58 – 200 mrad was used for imaging. Energy-dispersive X-ray spectroscopy (EDXS) mapping during STEM is enabled via a Dual Bruker XFlash 6 | 100 EDXS detector. The time series for the alloy formation was measured using this setup (see Fig. 3 and Fig. S4).

For all other STEM based analyses, STEM images were taken in a Thermo Fisher Scientific Spectra 200C-FEG microscope. The microscope was operated in STEM mode using a high-angle annular dark-field (HAADF) detector with a collection-angle ranging from 56 to 200 mrad, an acceleration voltage of 200 kV, a beam current of 120 pA, and a camera length of 98 mm. Energy-dispersive X-ray spectroscopy (EDXS) mapping during STEM is enabled via a Super-X detector G2 EDXS detector.

2.2.4. Mie theory calculations

The simulations of the optical properties were carried out based on the analytical solutions by the Mie theory. The MATLAB implementation used in this contribution is an adaption of the code by Jan Schäfer from the University of Ulm [34], which is based on the work of Wiscombe [35] and its modifications by Bohren and Huffman [36]. Mie calculations were performed for calibrating the population balance equation (PBE) model. The difference between the predicted and measured particle size and composition distributions was quantified by the distance of measured and simulated LSPR peak positions over time. The refractive index was taken from literature [37] and interpolated in terms of alloy composition and wavelength. Moreover, due to the small size of the alloy particles below 10 nm, corrections of the dielectric function were applied. The description of this finite size effect is well-described elsewhere [38–41]. A detailed comparison of calculated and experimentally acquired optical spectra can be found in the ESI of our recent publication [16].

3. Results and discussion

3.1. Hydrochemical equilibria

At the initial stage of the alloy formation, the gold and silver precursors are mixed with dextran as the reducing agent and NaOH to adjust the pH. Therefore, free silver (Ag^+), Cl^-, and OH^- are present in solution, which can form the poorly soluble salt AgCl (solubility product $K_{sp} \approx 10^{-10}$ mol^2L^{-2}) and/or AgOH (solubility product $K_{sp} \approx 10^{-8}$ mol^2L^{-2}) depending on the initial concentrations and the pH. In particular, the AgCl formation is known to limit the formation of AgAu ANPs [19,25]. To estimate the impact of the AgCl formation under the herein considered process conditions, we perform hydrochemistry calculations to quantify the distribution of chemical complexes under equilibrium conditions in water and deduce the supersaturation levels leading to the formation of AgCl and AgOH. More specifically, we solve a set of chemical equilibrium equations:

$$k_i = \prod_j \left(\gamma_j c_j\right)^{\nu_{ij}} \tag{1}$$

together with the conservation of mass, i.e.,

$$c_{total}(i) = \sum_j \mu_{ij} c_j, \tag{2}$$

where k_i, $c_{total}(i)$, c_j, γ_j, ν_{ij}, and μ_{ij} denote the equilibrium constants for the species i, the total ion concentration, the species concentration, the activity coefficient, the stoichiometric species coefficients, and the stoichiometric component coefficients, respectively. For details on how to solve the nonlinear set of equations, we refer to Hartig *et al.* [42] and Haderlein *et al.* [43]. The herein considered ions and complexes can be found in Table S1 in the ESI. The hydrochemical behavior of gold is still debated [11,44]. For the sake of simplicity, we assume that gold reduction and silver salt precipitation, which simultaneously takes place due to the contact of the gold precursor with the active reducing agent, are decoupled.

While the NP formation proceeds, Ag^+ ions from the liquid phase are embedded in the particle and, thus, are taken out of the hydrochemical equilibrium. To assess the supersaturation of AgCl and AgOH, we prescribe initially the precursor concentration of the different ions (Ag^+, NO_3^-, Na^+, OH^-, Cl^-, H^+). We keep all ion concentrations fixed except the silver ion concentration. Fig. 1a shows the supersaturation S for the two salts as a function of the prescribed total silver concentration $c_{total}(Ag)$. The supersaturation of each salt is calculated based on the free concentration of the two counter ions, for example for AgCl:

$$S = \pm\gamma \left(\frac{c_{Ag+} \bullet c_{Cl-}}{K_{sp}} \right)^{0.5} \tag{3}$$

where $\pm\gamma$ denotes the mean activity coefficient, which is assumed for the sake of simplicity as 1. Note that, without complex formation, the total precursor concentration and the free concentration are the same. Fig. 1a indicates that for the process conditions during the formation of ANPs with a molar gold content of 25 %, 50 %, and 75 %, AgCl is supersaturated while AgOH is undersaturated (see also Fig. S1). Thus, we can conclude that AgCl is the predominantly formed salt.

In a second step, we stoichiometrically extract silver and chloride ions (as solid) using a numerical method to obtain the condition $S = 1$ (bisection method). The resulting free silver concentration as a function of the total silver precursor concentration for different molar gold contents is shown in Fig. 1b. Note that, as the molar gold content is varied, not only the total silver concentration but also the total chloride concentration changes. Beyond $c_{total}(Ag) \approx 0.5\mu M$, AgCl is supersaturated which suggests a precipitation of AgCl (see Fig. 1a). The respective solid concentration c_s of AgCl for $S = 1$ is depicted in the ESI in Fig. S1. For $S > 1$, the free silver concentration c_{Ag^+} in solution is limited by the AgCl salt formation, which is evident from the plateau of c_{Ag^+} for $c_{tot}(Ag) \gtrsim 0.5\mu M$ (see Fig. 1b). The sharp crossover at $c_{total}(Ag) \approx 0.5\mu M$ indicates the transition from a supersaturated to an undersaturated state, which is underlined by a vanishing solid concentration (see Fig. S1).

We conclude that at the beginning of the alloy synthesis AgCl forms as a white precipitate (see Fig. S6a), which reduces drastically the available free silver concentration in solution. Hence, initially free gold ions (Au^{3+}) relative to silver ions (Ag^+) are in surplus, which favors the nucleation of gold rich nuclei and their molecular growth. Gradually, free silver ions in solution are reduced and integrated at the newly formed particle surface. To maintain the thermodynamic equilibrium, the solid AgCl redissolves and delivers further free silver ions for the alloy formation. The slow integration of silver ions into the gold rich particle over time becomes evident by the slow drop of the LSPR over time as seen in Fig. 4 and Fig. 8. We would like to emphasize that the evolution of the free silver concentration as a function of the total silver concentration (see Fig. 1b) acts as an important basis for the modeling of the alloy formation (see Equation (4) in section 4.6).

3.2. Microscopic analysis

In order to investigate the formation behavior of the silver-gold alloy NPs, HAADF-STEM and STEM-EDXS measurements were performed over the course of the reaction. For this, the slow reaction kinetics of the presented synthesis route was exploited and samples were taken over the course of the reaction. Fig. 2 shows HAADF-STEM micrographs of samples with a molar gold content of 20 %, 50 %, and 80 % taken seconds after the start of the reaction.

The images show cubic structures with an edge length of 100 – 200 nm, independent of the molar gold content, which can be identified as AgCl via elemental analysis (see Fig. S2 in the ESI). This supports the calculations presented in the previous section, which suggest a high supersaturation of AgCl due to the high total silver and gold precursor concentrations. In addition to the formation of AgCl crystals, an

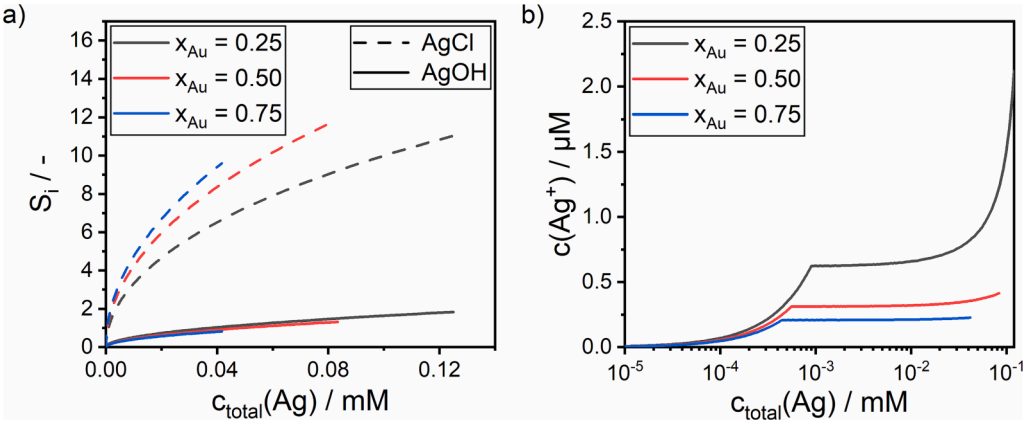

Fig. 1. (a) Supersaturation S_i as a function of the total silver precursor concentration $c_{total}(Ag)$ for different gold molar fractions x_{Au}. The nitrate and chloride concentration are kept constant: $c_{total}(NO_3^-) = 0.083$ mM and $c_{total}(Cl^-) = 4 \bullet 0.083$ mM. (b) The free silver concentration c_{Ag+} in solution as a function of the total silver precursor concentration $c_{total}(Ag)$ for different gold molar fractions x_{Au} after extracting the solid AgCl to obtain $S = 1$. (For interpretation of the references to color in this figure legend, the reader is referred to the web version of this article.)

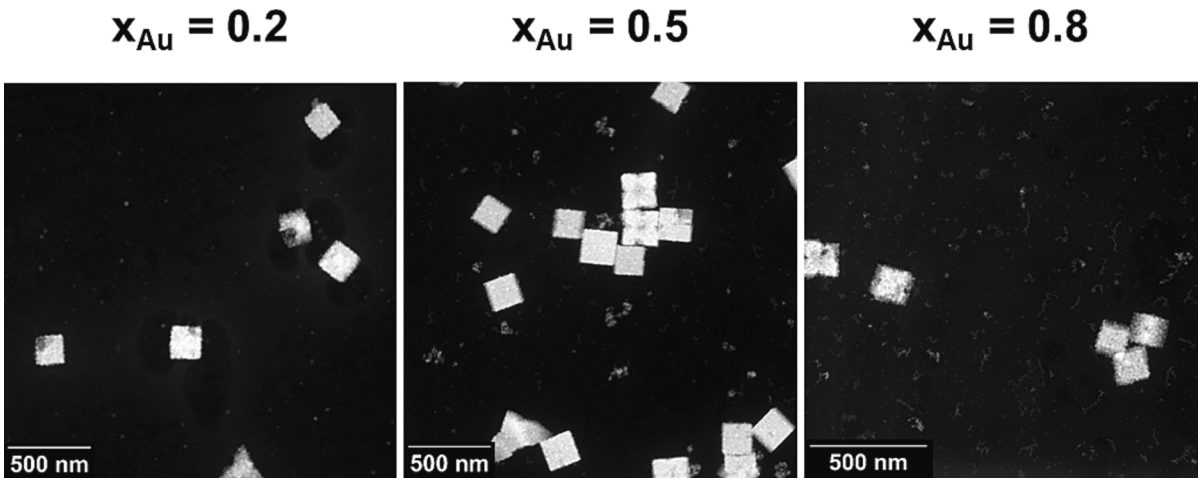

Fig. 2. STEM images of aliquots taken from the synthesis of silver-gold ANPs with a molar gold content of 20 %, 50 %, and 80 %. The samples were taken seconds after the start of the synthesis.

increasing number of small particles can be observed with an increase in the molar gold content. Evaluating the elemental compositions of these particles, the smaller particles are found to have a high gold content of almost 100 % (see ESI Fig. S2). This shows that in addition to the formation of AgCl crystals, the nucleation of the metal particles happens very early on in the synthesis. As most of the silver in the synthesis solution is precipitated as AgCl crystals, the formed nuclei almost exclusively consist of gold. Further, with an increasing molar gold content in the solution, the supersaturation of gold ions increases, leading to more formed nuclei, which can clearly be seen in the images.

When looking at the chemical composition of the AgCl crystals in more detail, a distinct gold signal can be found on the surface of the cubic crystals as well (see ESI Fig. S2). This suggests that in addition to the homogeneous nucleation of gold NPs in solution, gold deposits on the AgCl crystals.

To determine the origin of gold on the surface of AgCl crystals, we conducted zeta potential measurements on various suspensions. These included suspensions containing only AgCl, AgCl with dextran, and fully formed NPs without residual AgCl. The zeta potential of the synthesized ANPs was determined to be –32 mV. In comparison, the zeta potential of AgCl suspensions was measured as −34 mV and −9 mV in the absence and presence of dextran, respectively. Based on these observations, we can conclude that both AgCl and the NPs are adequately stabilized, making the aggregation of these entities unlikely. Therefore, the presence of gold deposits on the surface of AgCl crystals must be attributed to a nucleation and growth process rather than aggregation.

Crystallization can be divided in nucleation and growth. In the nucleation step, small and stable nuclei are formed, which act as seeds for the growth of final NPs. These nuclei then grow to their final size via a variety of growth mechanisms. Crystallization is driven by the supersaturation of the crystalizing component in solution, which also determines the temporal transition from the nucleation to the growth phase [45].

As the solubility of noble metals in water is extremely low ($\approx 10^{-12}$ molL^{-1} for gold [46]) and the concentrations used in our synthesis are comparably high for plasmonic NP syntheses [16], homogeneous as well as heterogeneous nucleation will occur in parallel. The heterogeneous nucleation on surfaces further depends on the involved surface energies [45], with edges of anisotropic structures usually showing higher surface energies [47–50]. This leads to a preferential nucleation of the metal atoms in solution at these spots. Through the application of a disproof-based method established by Finke *et al.* [51], we show that contrary to expectations, silver, rather than gold, predominantly undergoes heterogeneous nucleation on the surface of precipitated AgCl crystals. This finding can be rationalized by considering the distinct behavior of gold and silver in solution. Gold exhibits a significantly

higher supersaturation compared to silver, which favors homogeneous nucleation and consequently rapidly depletes the available gold atoms in solution. In contrast, the lower concentration of silver makes it more prone to heterogeneous nucleation. Moreover, in addition to reduction via dissolution according to the hydrochemical equilibrium, AgCl undergoes direct reduction from AgCl to Ag^0. As a result, free silver species are already present in close proximity to the AgCl crystals, enhancing the likelihood of heterogeneous nucleation events. The clearly visible gold deposits thus stem from the growth of gold onto the formed silver nuclei on the surface of the AgCl crystals. While such an unprecedently detailed analysis of the formation mechanism would hardly be possible based on experimental methods alone, we refer the reader to sections 3.6 and 3.7 where the strengths of our developed model are discussed.

The ratio of both nucleation pathways is proportional to the surface of AgCl present in solution, i.e., at lower gold concentrations more nuclei will be formed heterogeneously than homogeneously and vice versa.

For a molar gold content of 50 % additional samples were taken at reaction times of 9 h and 48 h. Fig. 3 shows the EDXS-maps of the full temporal sample series. Again, in the beginning of the reaction the previously discussed AgCl crystals are present. When AgCl crystals are irradiated by the electron beam of the electron microscope, elemental silver is formed [52], which can be seen as green spots in the available EDXS maps and explains the surplus of elemental silver in comparison to chloride in the net intensity plot.

After a reaction time of around 9 h, a core–shell structure can be observed in some particles with a gold-rich core and a silver-rich shell. This shows that indeed the process starts with the formation of highly gold-rich seed particles, which grow over time. This is expected, as most of the silver ions are complexed into scarcely soluble AgCl, which cannot participate in the reduction. The growth of the alloy particles, however, appears to be asymmetrical, i.e., gold and silver ions are not added at equal rates but sequentially. While several particles can be found, which show a core–shell structure, most particles that are seen on the spectrum images are in fact mostly alloyed (see Fig. S3). This firstly shows the asymmetrical formation behavior of the particles, but also that in addition to the reduction of silver and gold ions and their integration into stable nanocrystals, a reorganization within the formed crystals has to happen. At first, the concentration of metal in solution is so high that the surface growth rate exceeds the rate of intraparticle reorganization, resulting in core–shell structures. If the particles are kept in the dark throughout the reaction, the reaction rate of silver is, however, significantly reduced compared to a synthesis under light irradiation, providing the particles more time to mix internally. Thus, while core–shell structures are still observed, most of the particles are already alloyed at shorter reaction times. Details on the difference between both synthesis modes will be discussed in section 3.5.

At the final point of measurement after 48 h, the silver-gold ANPs with a mean particle size between 6 and 8 nm show no shell anymore. Only a slight enrichment of gold in the core of the particles and a slight enrichment of silver towards the outer spatial coordinate was observed. This effect is explained within our previous manuscript [16] and is generally in line with the literature on silver-gold ANPs produced in the liquid phase by chemical co-reduction [14,28,53,54]. It should be noted that while AgCl is present during the formation of the particles, no AgCl is found at the end of the synthesis. Further, the optical spectra of the final NP dispersions show no sign of other Ag species besides Ag^0 within the final NPs (see section 3.3).

In summary, the STEM-EDXS analysis clearly shows the growth of the NPs from an initial gold-rich core particle with a diameter of 2–3 nm in the early stage of the reaction to a final size of 6–8 nm. After the formation of a gold-rich core, this core is subsequently covered by a silver-rich shell, as most of the gold precursor in solution is already converted to gold core particles. Both metals, due to their almost identical lattice constants [21–23] and atom sizes [55], finally diffuse into each other and form a fully alloyed nanoparticle. Diffusional penetration of silver atoms into an existing gold crystal lattice at room temperature in the presence of chloride ions has been observed in the literature before and can be explained additionally by the reorganization of the crystal lattice due to defects and vacancies in the lattice and a following lattice reconstruction [56].

3.3. Evolution of the optical properties

The position of the LSPR of particle suspensions containing 7 nm silver-gold ANPs shifts between the position of suspensions containing pure silver NPs at around 400 nm wavelength to the LSPR position of pure gold NPs at around 520 nm [16,17]. The LSPR position thereby indicates the chemical composition at constant particle size, i.e., the molar gold content of the particles. It must be noted that while a correlation between the NP diameter and the LSPR position does exist, it is only observable for NP diameters above approximately 20 nm [57]. Since the particles produced within this study have a diameter below 10 nm, the shift in the LSPR must result from changes in their chemical composition. During the formation of the particles, the LSPR peak shifts from higher wavelengths around 500 nm to the final peak position of the respective particle suspension. The shift in the LSPR position can be explained by the shift in the chemical composition of the particles over time, from a position of particles with a high molar gold content towards a wavelength characteristic for the respective alloy NP suspension. Fig. 4a, b and c show this shift for three suspensions containing silver-gold ANPs with a molar gold content of 25 %, 50 %, and 75 %, respectively. Plotting the LSPR positions of the three suspensions over time, a decay can be observed, which over time converges to the expected LSPR positions for homogeneously alloyed particles with the three respective particle compositions at 426 nm, 450 nm, and 485 nm (see Fig. 8a).

This supports the behavior seen in the EDXS maps. The formation of the ANPs starts with the formation of highly gold rich nuclei, which grow to fully alloyed NPs. This can firstly be explained by the difference in the electrochemical potential of Au^{3+}/Au, Au^{+}/Au, and Ag^{+}/Ag. As gold is the more noble metal, it will be reduced first, leading to the formation of gold atoms in the solution and from there to gold clusters and nanoparticles rich in gold. Simultaneously however, as described in section 3.1, solid AgCl precipitates from the silver ions of the silver precursor and the chloride ions from the gold precursor. This leads to a strong decrease of the free silver ions, which are available for reaction, and further reduces the formation of silver ions to elementary silver. From the final LSPR values at the end of the formation process we can further conclude that an intraparticulate reorganization process is present. This is because the LSPR positions of core–shell particles would show values at higher wavelengths than their alloyed counterpart [58]. While the blue shift in the optical spectra over the course of the reaction is not only caused by the formation of alloys with shifting elemental compositions but by a simultaneous growth of a silver shell and diffusional mixing of the produced NPs, it is only possible to reach the values stated above if gold and silver atoms are fully mixed over the entire particle. At this point, we also mention that the formed particles are electrosterically stabilized via the adsorption of dextran molecules to the particle surface.

The formation of alloy NPs is reflected by the evolution of the extinction at the respective LSPR positions (Fig. 4d) (as well as the LSPR peak position), which can thus be seen as a measure for the effective alloy formation kinetics. The reaction rates and particle formation are correlated to several factors, including temperature, pH, and light illumination. The dependence on temperature can be explained by Arrhenius' law, which mainly influences the reduction reaction in the first step of the particle formation. Additionally, a correlation between the pH value within the reaction solution and the effective reaction rate can be observed, i.e., the higher the initial pH value, the faster is the particle formation (see Fig. S5a). This can be explained by the reaction mechanism of dextran, which is used as the reducing agent. As a reducing

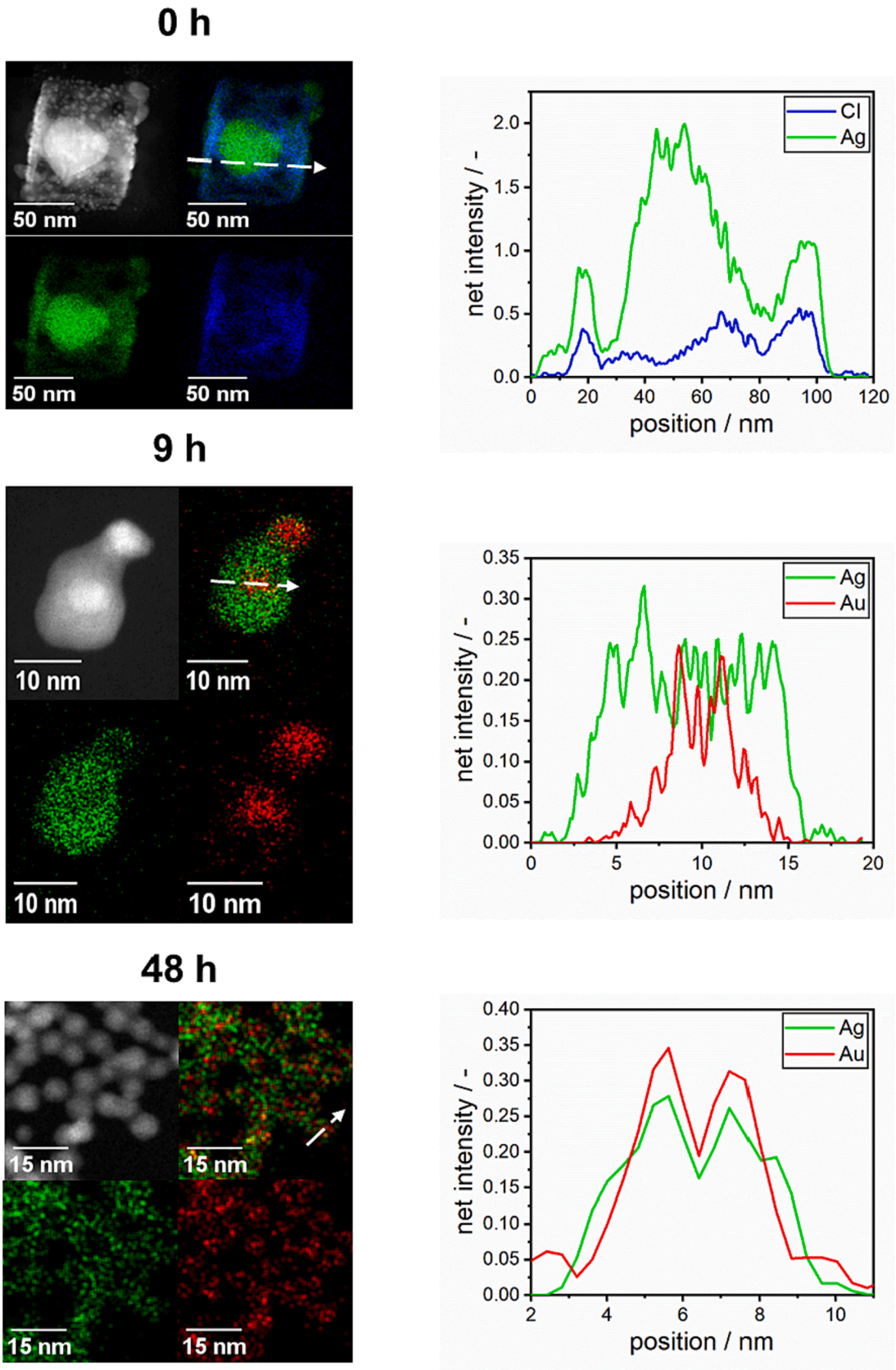

Fig. 3. Time-resolved STEM-images and -EDXS maps of silver-gold alloy NPs with a molar gold content of 50 %. Samples were taken in the beginning of the reaction (0 h), after 9 h of reaction and after the end of the reaction around 48 h. Respective elementary distributions are given in the diagrams on the right with the white arrow in the STEM-EDXS maps indicating the line scan. (For interpretation of the references to color in this figure legend, the reader is referred to the web version of this article.)

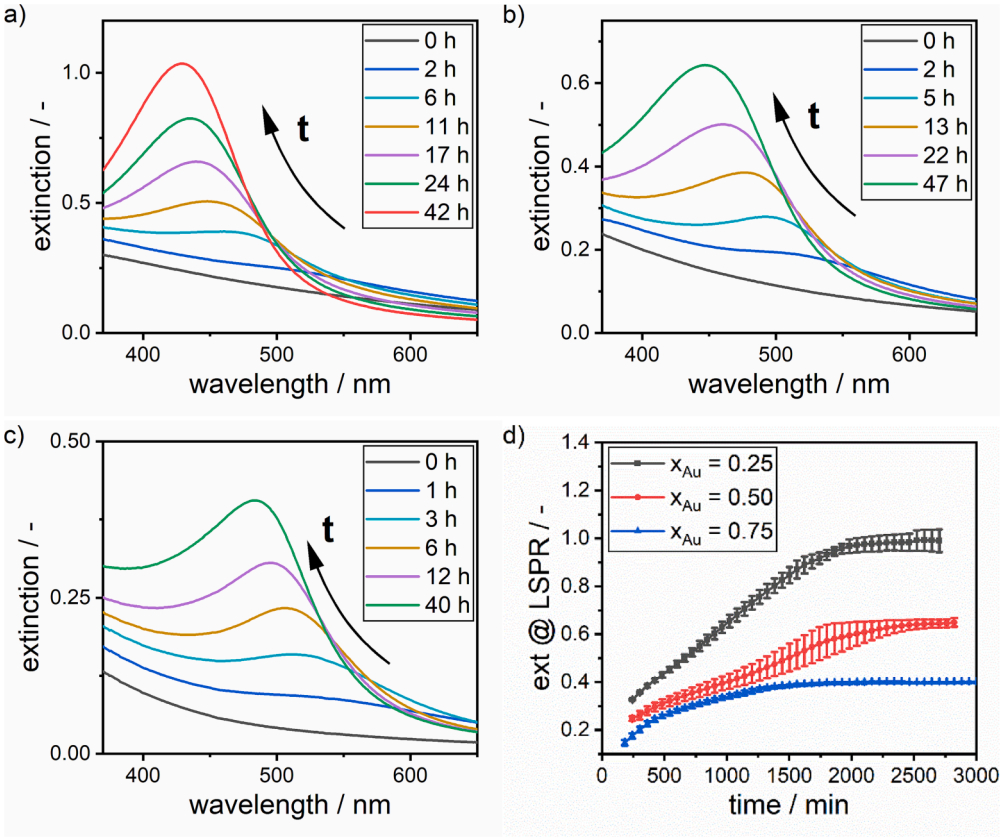

Fig. 4. (a-c) time-resolved extinction spectra of silver-gold ANPs with a molar gold content of 25 %, 50 %, and 75 % respectively. (d) corresponding extinction value at the LSPR position of silver-gold ANPs with a molar gold content of 25 %, 50 %, and 75 % over time. (For interpretation of the references to color in this figure legend, the reader is referred to the web version of this article.)

sugar, dextran mainly reacts via the oxidation of its terminal aldehyde groups [59,60]. These aldehyde groups need to be firstly converted to alkoxide groups, which then in turn reduce the metal ions in solution [61]. The higher the pH and thus the concentration of hydroxide ions, the more reactive groups are available for the dextran and thus the stronger the dextran is as the reducing agent. As the gold precursor used in this study is highly acidic, any difference in the precursor ratios directly affects the pH value of the reaction solution and thus the reaction rate. To mitigate this effect and observe the effects on the reaction rate solely from the difference in silver and gold concentration, the pH was adjusted to a fixed value of 11.1 for all compositions by adjusting the concentration of the added sodium hydroxide solution.

Within this study the temperature is kept constant at room temperature, the reaction is carried out in the dark and only exposed to monochromatic light during UV–Vis measurements and the initial pH is adjusted to the same value for all samples. This keeps most parameters well under control over the course of the reaction and yields highly reproducible results.

In addition, we demonstrated that the synthesis works in a similar manner in the presence of light (see section 3.5). This influence of light irradiation can be explained by the photo reduction of AgCl to elemental silver via light irradiation [62–64]. Thus, exposed to light, the particles are formed in approximately half the time compared to a synthesis in the absence of light [16].

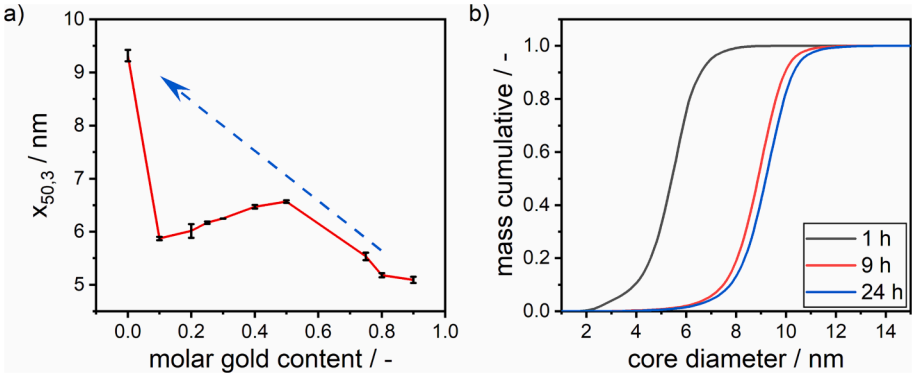

Fig. 5. (a) $x_{50,3}$ values derived via SV-AUC of the synthesized silver-gold ANP suspensions over their molar gold content. The blue dashed arrow highlights the expected growth trajectory of the NPs if no second nucleation process was present. (b) Cumulative PSDs for GSH-quenched silver NPs over the process time as derived by SV-AUC. (For interpretation of the references to color in this figure legend, the reader is referred to the web version of this article.)

3.4. Particle size distributions

PSDs of the particle suspensions were measured via SV-AUC experiments and confirmed by STEM image analysis (see ESI Fig. S7). Following our previously reported results [16], a dextran shell thickness of 2.3 nm was taken into consideration for the calculation of the core diameter distributions. This value is assumed constant for all alloy NPs, independent of their molar gold content. Fig. 5a shows the mass median value ($x_{50,3}$) over the molar gold content of the final particles. Noticeably, as pure gold particles exhibit a different but also complex formation behavior (see ESI Fig. S9), results for pure gold NPs have been excluded for all measurements and simulations.

A clear trend in particle size can be observed as the molar gold content decreases, with a local maximum around 50 % molar gold content and a global maximum for pure silver particles. This non-monotonous behavior is a clear indication of more than one mechanism influencing the nucleation of the formed NPs. Since gold plays a predominant role in nucleating the particles, the concentration of gold in the reaction mixture directly influences the nucleation rate, consequently, the number of formed nuclei and with it, the final particle size. Therefore, at high gold contents, there is a high supersaturation of gold precursor, resulting in a higher reduction rate and homogeneous nucleation rate, leading to smaller particles. As the molar gold content decreases, the homogeneous nucleation rate follows the concentration of gold in solution, leading to fewer nuclei and consequently a decrease in particle formation and an increase in particle diameter. Without an additional effect, which influences the nucleation behavior of the system, one would expect a further, monotonous increase of the mass median value with further decreasing molar gold content (see blue dashed arrow), as fewer and fewer nuclei are present in solution. Therefore, a second process must be present, which increases the number of available nuclei at higher silver contents. We conclude that this process must be heterogeneous nucleation on the readily available surface of the AgCl crystals. The heterogeneous nucleation rate is associated with the total surface area of AgCl crystals in solution, which increases as the gold content decreases and the silver (chloride) content increases. It is important to notice that for pure silver NPs no AgCl is formed as no gold precursor (Cl^- ions) is present. Therefore, no heterogeneous nucleation can occur and the size of pure silver particles follows the trend observed for NPs with a molar gold content below 50 %.

These combined effects cause a shift in the mean particle size towards smaller particles at both higher and lower gold contents. Consequently, a maximum in particle size occurs at a molar gold content of 50 %. This happens because the combination of homogeneous nucleation, which dominates at high molar gold contents, and heterogeneous nucleation, which dominates at low molar gold contents, is the weakest at this composition. The non-monotonous increase in the particle size thus arises from a complex interplay between homo- and heterogeneous nucleation of the alloy NPs.

Further, to gain a better understanding of the growth behavior of the formed NPs, we conducted an analysis of the PSDs of pure silver NPs using PSD measurements (refer to Fig. 5b). To accomplish this, we halted the reaction at different time intervals (1 h, 9 h, and 24 h) by introducing Glutathione (GSH). It has been recently reported by our research group that GSH has the ability to arrest the growth of noble metal NPs by binding irreversibly to their surfaces [65]. Accordingly, to retrieve core diameter distributions, a GSH shell thickness of 0.86 nm was used as reported in the latter publication.

The obtained PSDs exhibit a noticeable shift over time, with the most significant shift occurring early in the reaction, followed by a slowed growth rate towards the later stages of the process. Interestingly, the shape of the cumulative distribution remains unchanged throughout the synthesis (see ESI Fig. S8). The corresponding function can be described by a lognormal distribution with a mean particle size of 5.6 nm, 9.0 nm, and 9.3 nm for a reaction time of 1 h, 9 h, and 24 h, respectively, and a constant standard deviation of 0.9 nm. This consistent behavior implies a size-independent growth mechanism for the NPs with an effective mean growth rate of 0.4 nm h^{-1} for the interval between 1 h and 9 h of reaction time and accordingly implies the surface reaction of the monomers to be the limiting factor for the crystal growth [66]. This is consistent with the slow formation kinetics and is in contrast to the faster diffusion limited growth.

3.5. Proposed formation mechanism

Based on the findings from the measurements and calculations above, a sequence of steps and mechanisms for the formation of the silver-gold ANPs is proposed (see Fig. 6). In a first step, we assume that mixing of the precursors controls the precipitation of sparingly soluble silver chloride NPs. The low solubility of AgCl strongly reduces the driving force to form silver NPs. However, AgCl serves as a reservoir for the slow incorporation of silver into the alloy and is reduced directly to Ag^0 at a low reaction rate. The amount of silver in the AgCl crystals depends on the precursor concentrations, the precursor ratios of silver and gold, the reaction temperature, and the pH. In the second step, mainly Au ions and to a minor extent Ag ions in the solution are reduced by the reducing agent dextran to gold and silver atoms. These atoms subsequently form stable nuclei in the first part of the alloy formation. Nuclei can be formed via homogeneous as well as heterogeneous nucleation. Homogeneous nuclei consist of mostly gold. To a minor extent, depending on the intended final molar gold content and thus the portions of silver and gold precursor in the reaction mixture, also mixture AgAu or even Ag nuclei might form. These are considered as side reactions and will not be considered in our model. Heterogeneous nuclei reversely consist of mostly silver and to a minor extent also of AgAu and Au. According to the disproof-based method described above, it was established that the formation of heterogeneous AgAu and Au nuclei happens so scarcely that they will not be considered in our model. In the following growth step, the remaining ions in solution are reduced and are integrated into the crystal lattice. The growth of the particles is found to be size independent and surface reaction controlled as seen from the long reaction times and the PSDs over time (see Fig. 5b), where the shape of the PSD does not change. By reducing the silver ions in solution, the chemical equilibrium within the dispersion is shifted, Ag ions are released from the AgCl, reduced and integrated into the alloy. This process continues until no AgCl is present anymore. In addition, AgCl is reduced directly to Ag^0 with a much slower reduction rate than the Ag ions in solution and thus adds to the formation of Ag^0 [67]. While we consider the subsequent change in the chemical equilibrium to be

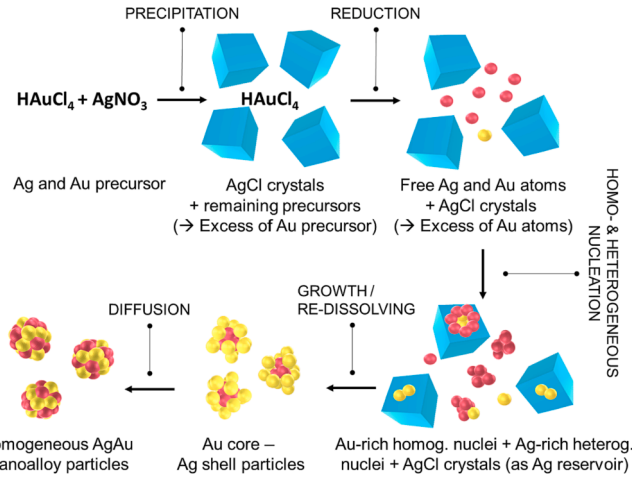

Fig. 6. Proposed formation mechanism for the formation of silver-gold ANPs via the previously established synthesis [16] using dextran as the reducing and capping agent. (For interpretation of the references to color in this figure legend, the reader is referred to the web version of this article.)

instantaneous in each time step, we describe the dissolution of the AgCl crystals due to the direct reduction to Ag^0 via a negative growth rate.

The AgCl crystals therefore effectively act as a silver reservoir, successively dissolving while Ag atoms are formed. A similar behavior has been described in literature before for AgBr particles acting as an Ag reservoir during the growth of a silver shell around gold rods [68]. Thus, most of the ions being reduced on the surface of the gold-rich core NPs are silver ions. The observed silver shell around the gold cores is a consequence of the stepwise and decoupled reduction of gold and silver. These core–shell particles finally undergo diffusional mixing and the NPs effectively undergo the transition from a core–shell particle to a fully alloyed NP. The intermixing of gold and silver at room temperature has been described in literature before and can be accredited to defects in the crystal structure of the core particle [56]. While Fig. 6 presents the formation of the ANPs as 6 subsequent steps, it must be noted that all steps run simultaneously and are strongly connected.

It should be noted that as mentioned in the sections before, the formation of the particles is significantly affected by light irradiation. Specifically, the formation rate of the particles is increased by around a factor of two from 30 to 50 h to 15–20 h (see Fig. S4). This can be explained by the photo reduction of AgCl to elemental Ag^0, which is a typical process known in literature [62–64]. More details are given in the ESI.

3.6. From experimental observations to a general population balance model for the alloy formation

Based on the experimental observations, we aim for developing a model, which accounts for the most relevant formation steps of the alloy particle formation. The core of the model is a multi-dimensional PBE:

$$\dot{q}(t,\boldsymbol{x}) + \nabla_{\boldsymbol{x}}\cdot(\boldsymbol{G}(\boldsymbol{c},\boldsymbol{x})q(t,\boldsymbol{x})) = 0 \tag{4}$$

describing the spatiotemporal evolution of the number density function q. The dispersed phase vector $\boldsymbol{x} = (r, x_{\mathrm{Au}})$ consists of the particle radius r and the volume fraction of gold atoms x_{Au}. We assume that each noble metal has its own growth rate written in a general form $G_i(c_i) = k_{g,i}(c_i - c_{eq,i})r^n$, which depends on the growth constant $k_{\mathrm{g,i}}$, the local solute concentration c_{i} as well as the equilibrium concentration $c_{\mathrm{eq,i}}$ of the i^{th} noble metal and the particle radius of a formed NP, r. The exponent n depends on the growth mechanism. The solubility of noble metals is negligibly small [46], such that the approximation $c_i - c_{eq,i} \approx c_i$ can be assumed valid. The growth term for radii $r > r_{\mathrm{nucl}}$, where r_{nucl} describes the radius of the formed nuclei, and molar gold contents $x_{\mathrm{Au}} \in [0,1]$ reads:

$$\boldsymbol{G}(\boldsymbol{c},(r,x_{Au})) = \begin{pmatrix} (G_{Au}(c_{Au}) + G_{Ag}(c_{Ag}))r^n \\ 3(G_{Au}(c_{Au})(1-x_{Au}) - G_{Ag}(c_{Ag})x_{Au})r^{n-1} \end{pmatrix} \tag{5}$$

A detailed derivation of the growth rate expression can be found in Muneer *et al.* [69]. The formation of new nuclei with the critical radius r_{nucl} is prescribed in the PBE by a nucleation boundary condition. The nucleation rate is given by:

$$N(c_{Au},c_{Ag},A_{AgCl}) = \frac{N_{Au}^{hom}(c_{Au}) + N_{Ag}^{hom}(c_{Ag}) + N_{Ag}^{het}(A_{AgCl},c_{Ag})}{r_{\mathrm{nucl}}^n(G_{Au}(c_{Au}) + G_{Ag}(c_{Ag}))} \tag{6}$$

where homogeneous nucleation N^{hom} of Au and Ag nuclei as well as heterogeneous nucleation N^{het} of Ag nuclei on the AgCl surface (A_{AgCl}, describing the surface area of all AgCl NPs) are modeled by the classical nucleation theory as prescribed by Mersmann *et al.* [70]. The average composition of the precipitated nuclei is given by the ratio of the nucleation rates – assuming a constant nuclei size – i.e.,

$$x_{\mathrm{Au,\ nucl}}(\boldsymbol{c}) = \frac{N_{Au}^{hom}(c_{Au})}{N_{Au}^{hom}(c_{Au}) + N_{Ag}^{hom}(c_{Ag}) + N_{Ag}^{het}(A_{AgCl},c_{Ag})} \tag{7}$$

Altogether, we obtain the following boundary condition accounting for nucleation:

$$q(t,(r_{\mathrm{nucl}},x_{Au})) = N(c_{Au},c_{Ag},A_{AgCl})\delta_0(x_{Au} - x_{\mathrm{Au,\ nucl}}(\boldsymbol{c}))\forall t > 0, x_{Au} \in [0,1] \tag{8}$$

The postulated PBE model for alloy particles is subject to several assumptions. First, we neglect a dependence of the growth rate on the surface composition. This means that gold and silver atoms are integrated at the same rate into both a gold-rich and silver-rich particle surface. Thus, the composition along the radial axis of the particle is mainly determined by the ratio between the precursor reduction rates, the nucleation rates and growth rates of each noble metal as emphasized in Equation (6) and (7). The same approach is inferred for the nucleation of the alloy nuclei. The ratio between the single nucleation rates of each noble metal determines the mean composition $x_{\mathrm{Au,nucl}}$ of the formed nuclei. Analysis of the multi-dimensional population balance equation shows that the strong dependence of nucleation rate on solute concentration leads to preferential formation of the rate-dominant substance. Only when the nucleation rate of each metal is in the same order of magnitude, an alloy nuclei formation would occur. Due to the highly nonlinear dependence of the nucleation rates on the solute concentrations, the likelihood that the nucleation rates of both noble metals remain on a similar level for an extended period of time is small. Hence, in the most cases $x_{\mathrm{Au,nucl}}$ is either ≈ 1 (in the presence of Au) or ≈ 0 (in the absence of Au).

The PBE model is complemented with a mass balance:

$$\boldsymbol{c}(t) = \boldsymbol{c}_{in}(t) - \frac{4\pi}{3}\int_0^1\int_{r_{\mathrm{nucl}}}^{\infty}\begin{pmatrix}\rho_{Au}M_{Au}^{-1}x_{Au}\\ \rho_{Ag}M_{Ag}^{-1}(1-x_{Au})\end{pmatrix}r^3 q(t,(r,x_{Au}))\mathrm{d}r\mathrm{d}x_{Au} \tag{9}$$

where the term $c_{in}(t)$ denotes a time dependent external mass addition, ρ_{Au} and ρ_{Ag} describe the density of Au and Ag, respectively, and M_{Au} and M_{Ag} the molar mass of Ag and Au respectively.

The first step in the synthesis of noble metal particles is the reduction of the metal ions to the elementary oxidation state. We here rely on the simplest case of one component reduction from a trivalent Au ion, directly to the respective Au atom, which reads as:

$$\mathrm{Au}^{3+} \overset{k_{r,Au}}{\rightarrow} Au^0 \tag{10}$$

$$\mathrm{Ag}^{+} \leftrightarrow AgCl \tag{11}$$

$$\mathrm{Ag}^{+} \overset{k_{r,Ag}}{\rightarrow} Ag^0 \tag{12}$$

$$AgCl \overset{k_{r,AgCl}}{\rightarrow} Ag^0 \tag{13}$$

$$\frac{\mathrm{dAu}^{3+}(t)}{\mathrm{d}t} = -k_{r,Au}\mathrm{Au}^{3+}(t) \tag{14}$$

$$\frac{\mathrm{d}Au^0(t)}{\mathrm{d}t} = k_{r,Au}\mathrm{Au}^{3+}(t) \tag{15}$$

$$\frac{\mathrm{dAg}^{+}(t)}{\mathrm{d}t} = -k_{r,Ag}\psi_{Ag^+}(\mathrm{Ag}^{+}(t),\mathrm{Cl}^{-}(t)) - k_{r,AgCl}A_{AgCl}(\psi_{AgCl}(\mathrm{Ag}^{+}(t),\mathrm{Cl}^{-}(t))) \tag{16}$$

$$\frac{\mathrm{d}Ag^0(t)}{\mathrm{d}t} = k_{r,Ag}\psi_{\mathrm{Ag}^+}(\mathrm{Ag}^{+}(t),\mathrm{Cl}^{-}(t)) + \mathrm{k_{r,AgCl}A_{AgCl}}(\psi_{\mathrm{AgCl}}(\mathrm{Ag}^{+}(t),\mathrm{Cl}^{-}(t))) \tag{17}$$

where $\psi_X(\mathrm{Ag}^+,\mathrm{Cl}^-)$ denotes the concentration of $X \in \{AgCl, \mathrm{Ag}^+\}$ based on the ion concentrations of Ag^+ and Cl^- under hydrochemical equilibrium. We want to stress that more complex redox reactions can be straightforwardly implemented in the model by either incorporating – if decoupled – the analytical solution or the numerical solution as a mass

addition term c_{in} or by directly coupling the chemical equilibria to the mass balance stated in Equation (9). The multi-dimensional PBE with the mass balance is numerically solved by the recently developed multidimensional exact method of moments [69], which is based on a reformulation of the PBE in terms of a fixed-point-equation for the evolution of the concentrations. This is possible as, for given concentrations, the PBE solution can analytically be solved by the method of characteristics, see e.g., Keimer *et al.* [71], and was already introduced for the 1D case by Pflug *et al.* [72]. This analytical solution is then plugged into the mass balance in Equation (9) resulting in two one-dimensional nonlinear integral equations, which can be efficiently solved by numerical schemes.

The introduced PBE describes the formation of composite particles based on the mass transfer of ions from the bulk to the surface and their integration into the particle. However, due to the mobility of the metal atoms within the metal lattice, reorganization of the metal atoms within the particle can occur. This reorganization process can be enhanced by different defects of the solid phase such as point, line or planar defects (refer to chapter 3.5). The rates of the reorganization process and the reduction of silver then determine the morphology of the formed NPs, i.e., in the case of a high silver reduction rate and a low rate of reorganization, core–shell particles are formed, while for the opposite scenario, homogeneously mixed particles can be observed throughout the entire formation process. As discussed above, light plays an important role in the reduction of AgCl and significantly increases the reduction rate according to Eq. (13). Thus, under the influence of light irradiation, a clear formation of core–shell particles is observed (see Fig. S4). While the formation of core–shell particles can still be observed under light exclusion, it is much less pronounced, resulting in most particles showing a gradient in the composition over the radial dimension instead of a sharp boundary from silver to gold (see Fig. S3). This complex reorganization process exceeds the scope of our work for now and is thus neglected. As the expected change in the optical properties due to the slightly inhomogeneous distribution of both elements over time is marginal, we instead assume instantaneous mixing and thus a homogeneously mixed particle with varying size and molar gold content over time.

3.7. Quantitative modeling of alloy formation

In this section, we attempt to quantitatively model the formation of silver-gold ANPs using dextran as a reducing agent. However, the reduction rate constants, nucleation rate constants, and growth rate constants are unknown. We follow the approach of model-based material parameter estimation using global optimization to determine presumably unique solutions for the aforementioned constants. The extinction spectra measured experimentally over time (see Fig. 4), the PSDs from the final state based on AUC experiments (see Fig. S7 and Fig. 7), the $x_{50,3}$ values at different molar gold contents (see Fig. 5a), the evolution of the PSD of pure Ag NPs over the process time (see Fig. 5b), and the EDXS maps of the particles at certain process times (see Fig. 3) serve as optimization criteria here.

To compare the experimental data with the results of the described model, the rate and unknown material constants have to be determined. These constants should be unique from a physical point of view. If no unique solution can be found, further unknown dependencies might be present, which then would have to be resolved. To do so, we performed a simulated annealing type scheme [73] with more than 90 000 parameter combinations. This is important to rule out that we have an indeterminate system, i.e., to make sure that we have enough data to accurately fit

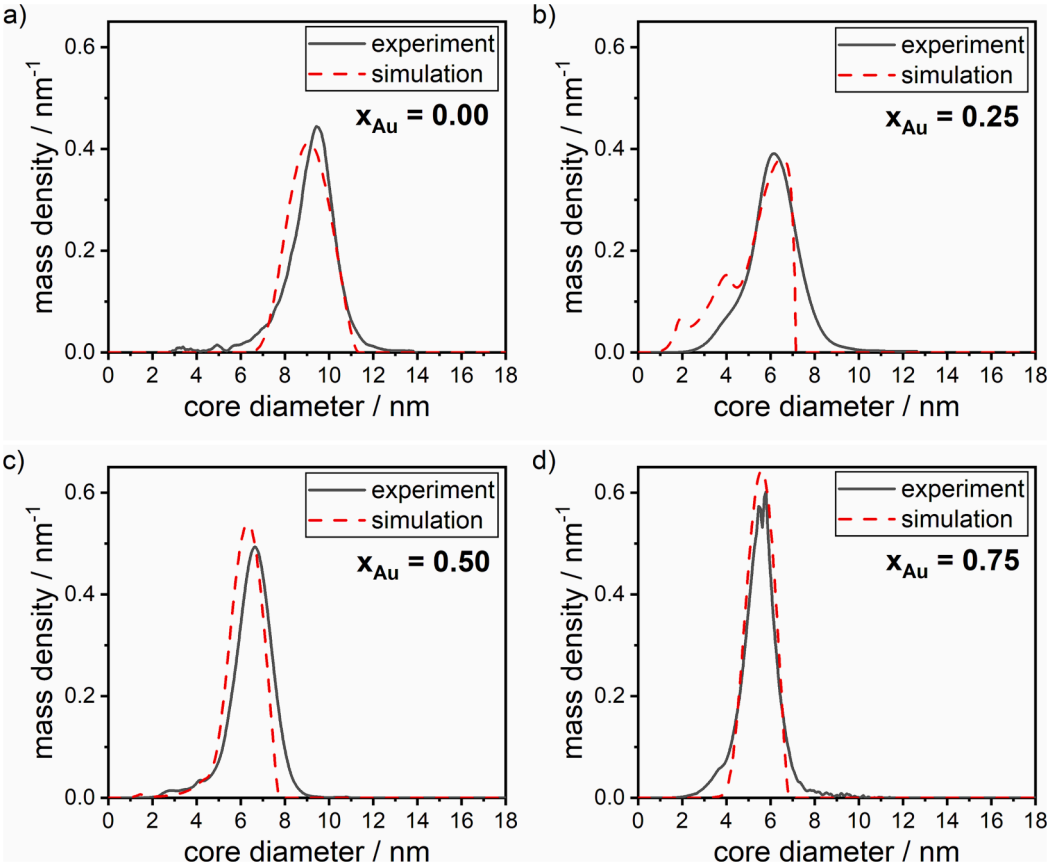

Fig. 7. Comparison of experimental (from SV-AUC experiments) and simulated mass density distributions for molar gold contents of 0 to 0.75 in steps of 0.25 from (a) to (d) respectively. Experimental data is shown in gray solid lines, while simulated curves are shown in red dashed lines. (For interpretation of the references to color in this figure legend, the reader is referred to the web version of this article.)

all of the 9 parameters and allows for statistical analysis as shown in Fig. S10. In the plots, a very narrow range of possible solutions can be found, clearly proofing that a reasonable unique solution in terms of a well-defined set of parameters does exist. The modal values as well as the corresponding standard deviations (from Fig. S10) for the parameters can be found in Table 1.

This approach is clearly superior to standard parameter fitting procedures such as least squares, as it provides information on the accuracy and uniqueness of the obtained parameters. Traditional approaches result in a single parameter set that does not provide insight into other potential formation pathways or solutions, whereas our approach clearly identifies all possible parameter combinations satisfying a given error bound. This can be used to identify unknown parameter correlations and to assess whether the data sets used are rich enough to identify the model parameters. In other words, our approach provides both novel insights into the formation pathway and allows to determine experimentally hardly accessible information, including kinetic constants, surface energies and solubilities.

Here, k_V describes the Mersmann constant [74] for the respective metal used to calculate the interfacial energy, which severely affects the nucleation rate. $c_{Ag,het}$ is a parameter from classical nucleation theory and is dependent on surface diffusion, the surface properties of Ag and AgCl, the adsorption of Ag on AgCl, the size of the formed nuclei and the concentration of silver in solution (see [70] – Table 1). Finally, f_{Ag} is a measure for the wettability of AgCl by Ag. The smaller f becomes the better the wettability and thus the better the interaction of the two materials, here Ag and AgCl [75].

The obtained parameters are hardly measurable experimentally and, in particular, for a silver-gold alloy NP system none are reported. However, a comparison of the estimated parameter values with literature values for similar systems allows an assessment in terms of physical meaningfulness. Reduction rate constants for silver and gold have been reported in a wide range, highly dependent on the reducing agent and other process parameters. Additionally, most rates found in literature are essentially observed effective rates including the whole particle formation process. Some values found are in the range of 10^{-3} s^{-1} and 10^{-5} s^{-1} [76–80]. The obtained reduction rate constants are thus definitely in the right range of values. Further, a higher value for the reduction rate constant of gold can be explained with the higher electrochemical potential of gold ions [81] compared to silver ions [82,83]. The reduction rate constant of AgCl accounts for the surface area of the available AgCl and its concentration. To make the value comparable to the rate constants of Ag and Au, one can calculate an equivalent rate for a given molar amount and surface of AgCl. As an example, in the beginning of the process, we observe cubic AgCl crystals with an edge length of approximately 180 nm, which amounts to a total surface of $2.8 \bullet 10^{-6}$ m^2L^{-1}. With knowledge of the initial molar amount of AgCl present in solution of $8.3 \bullet 10^{-5}$ molL-1, one can calculate the initial equivalent rate constant. This equivalent rate constant amounts to $1.1 \bullet 10^{-5}$ s^{-1}, which is much lower than that of pure silver and gold. This can again be explained by the much lower electrochemical potential of AgCl/Ag [84] compared to silver and gold ions.

Mersmann constants, which are a measure for the nucleation of the NPs and are proportional to the surface energy of the metal NP as well as its solubility, have been reported in the range of 0.31 to 0.414 [74,75]. However, large standard deviations of up to 400 % are reported with it [74], showing that the values found in this work are well within the expected range. Further, the Mersmann constants of silver and gold show similar values. The Mersmann constant is directly proportional to the surface energy as well as the solubility of the nucleating component (here silver and gold). While silver shows a lower surface energy than gold [85], its solubility is higher. This stems from the lower melting temperature of silver [86], which shows a lower cohesion energy, which finally shows a higher solubility, an effect that gives silver its antibacterial properties [20]. Thus, the lower surface energy of silver is canceled out by its higher solubility, leading to almost identical Mersmann constants for both components. With all other constants verified, the growth rate constant directly reflects the measured growth rate of the NPs (see Fig. 5b) and thus directly stems from experimental values.

In summary, we show that the parameters used in the model are in fact physically based parameters, which are determined via the presented approach. The obtained values are reasonable and can be explained via physical relationships. Fig. S5 indicates that the formation kinetics is additionally influenced by the initial pH of the solution. To account for this effect, we adjusted the initial pH value for all solutions to 11.1. Further, we assume that the reaction constants are not affected by the small variations in the pH during the reaction. With the calibrated model at hand, we now aim for quantitative comparison of experimental data with the data generated via the model.

Fig. 7 shows the comparison of the mass weighted PSDs at the end of the reaction for molar gold contents of 0 to 75 % in steps of 25 %. Three samples were measured for each molar gold content via SV-AUC, which are shown as a mean gray solid line. Firstly, a change in the modal values dependent on the molar gold content is evident again (see also Fig. 5), validating our assumptions. Further, monomodal distributions are found for all molar gold contents with excellent agreement between the experimental and the simulative data over both, the modal value and the width of the PSD. While agreement of the modal value can indeed be achieved even if the modelled formation mechanism is incorrect, the correct prediction of the PSDs for various compositions strongly supports the underlying mechanism [51].

With the particle dispersities well aligned, we look towards the optical properties, i.e., the extinction spectra of the final NP suspensions. The two-dimensional population balance equation provides information about the particle size and composition distribution, but no optical information. To compare the experimentally measured extinction spectra with the underlying simulated two-dimensional population density function, we convert the dispersed phase properties into optical information using Mie theory (see section 2.2.4 and Cardenas Lopez *et al.* [58] for details). More precisely, to numerically approximate the extinction of a size and composition distribution, the size distribution is first divided into small fractions. The extinction spectra of each fraction for an average size and composition are then accumulated to one final spectrum based on the number of particles in each fraction.

Fig. 8 depicts the comparison of the experimentally determined optical information with the simulatively generated data using the calibrated model. Fig. 8a thereby shows the position of the LSPR peaks over the course of the formation. The experimental data are combined with error bars, including the standard deviations in the measurement data from 3 measurements for each composition as well as the uncertainty in the determination of the peak maximum. To account for the uncertainty in the peak maximum, we assume a deviation in the maximum extinction at the LSPR position by 1 %. We then calculate a combined standard deviation assuming an equal distribution over the resulting span of peak positions.

Table 1
Determined parameters and standard deviations for the described model. The standard deviations correspond to the probability distributions for a deviation of 10 % from the optimal value (see Figure S10). As the parameters are based on physical constants, the values hold physical meaning.

Parameter	Optimal value
$k_{r,Au}$ / s^{-1}	$(10.0 \pm 0.2) \bullet 10^{-4}$
$k_{r,Ag}$ / s^{-1}	$(3.46 \pm 0.06) \bullet 10^{-4}$
$k_{r,AgCl}$ / mol m^{-2} s^{-1}	$(3.3 \pm 0.1) \bullet 10^{-4}$
$k_{V,Au}$ / -	0.1905 ± 0.0003
$k_{V,Ag}$ / -	0.1783 ± 0.0003
$c_{Ag,het}$ / m^{-2}	19285.87 ± 0.05
f_{Ag} / -	0.0301 ± 0.0003
$k_{g,Au}$ / m L s^{-1} mol^{-1}	$(1.12 \pm 0.03) \bullet 10^{-6}$
$k_{g,Ag}$ / m L s^{-1} mol^{-1}	$(1.46 \pm 0.03) \bullet 10^{-6}$

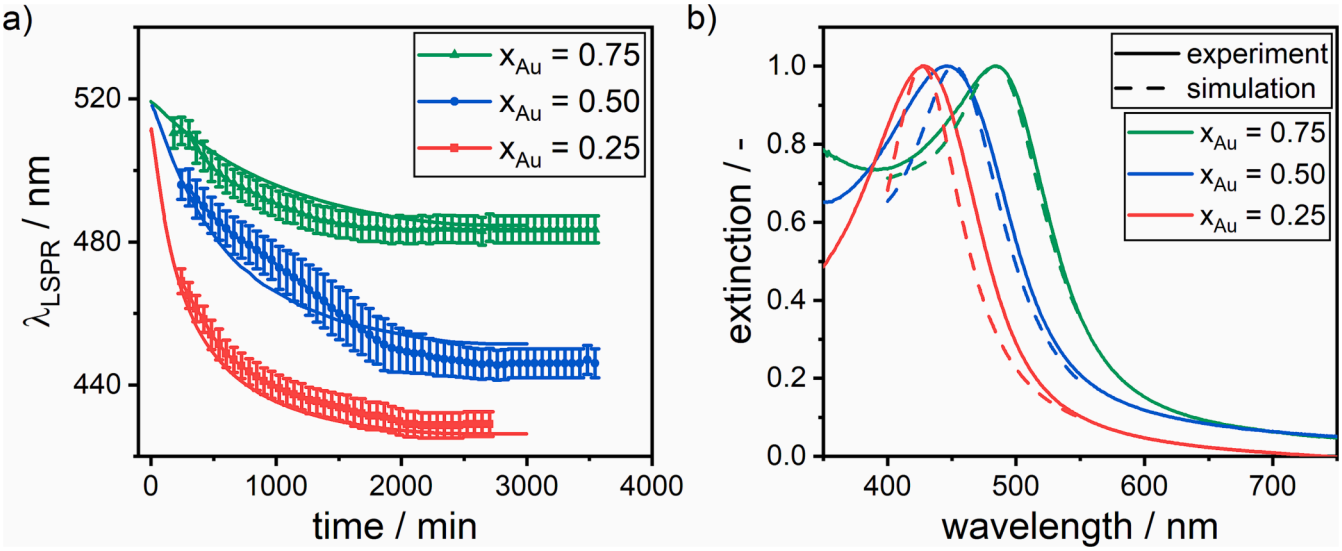

Fig. 8. (a) Comparison of experimental LSPR positions over time for different initial gold molar fractions with the simulated results. Experimental values are shown with error bars, while simulated values are shown as solid lines. (b) Corresponding comparison of normalized extinction spectra of the final particle suspensions after the end of the process with simulated results. Dashed lines show the experimental values, while solid lines symbolize the simulated curves. (For interpretation of the references to color in this figure legend, the reader is referred to the web version of this article.)

The solid lines indicate the predicted values, obtained from simulations. The plots show that, as described before, the formation starts with the formation of highly gold rich NPs, indicated by an initial LSPR position of around 520 nm, which is typical for such small gold NPs. Depending on the precursor ratio of silver and gold, the initial position gets closer to 520 nm with an increasing gold precursor ratio. Over the course of the experiment, the values exponentially decrease to a final value, which is indicative for the final molar gold content of 25 %, 50 %, and 75 % of the produced NPs. The simulated trend of the LSPR peak position shows good agreement with the experimental data over the course of the entire reaction and hits the final LSPR positions almost perfectly. When looking at the final extinction spectra at the end of the process (see Fig. 8b), very good agreement between the experimental data and the simulations is observed again in terms of the peak position, as well as the width of the peak. For the simulations, dampening due to the small size of the final NPs, which is too small for classical Mie theory

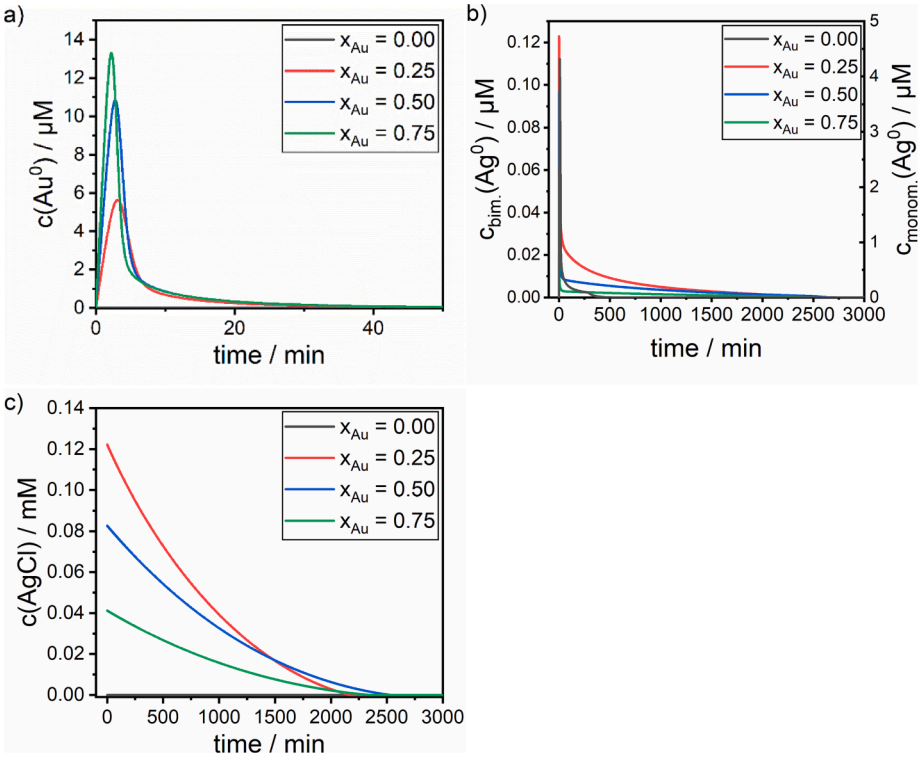

Fig. 9. Concentration of gold atoms - Au^0 (a) – and silver atoms - Ag^0 (b) - in the synthesis solution. As the concentration of silver atoms is much higher for monometallic silver, the concentration was plotted against a second y-axis. (c) Concentration of precipitated AgCl in the synthesis solution. (For interpretation of the references to color in this figure legend, the reader is referred to the web version of this article.)

has been taken into account (see [58;16]).

In summary, we find excellent quantitative agreement between experimental and simulated data, proofing a detailed understanding of the formation mechanism of the AgAu ANPs. With a calibrated model delivering physically grounded and correct values, we can use the model to extract additional data from the process, which are experimentally not accessible.

Fig. 9 shows the evolution of the concentrations of the considered Ag and Au species in time, with Fig. 9a depicting the evolution of Au^0 over time, Fig. 9b the evolution of Ag^0 and Fig. 9c the evolution of AgCl. Both Ag and Au atom concentrations show a spike in the beginning of the process due to the high concentration of precursors, causing a rapid reduction reaction. Afterwards, the concentration of both species is depleted via the following nucleation reaction, forming stable nuclei from the formed atoms. While gold atoms are depleted much faster, within the first hour of the reaction, silver atoms are present for more than 40 h. This is due to the precipitation of AgCl in the beginning of the process and its subsequent redissolving over time, which can also be seen from the concentration of AgCl over time in Fig. 9c. Here the concentration of AgCl runs out shortly before the concentration of silver atoms, validating our assumption. Additionally, we notice a significantly higher peak concentration of Au^0, compared to Ag^0, which is in line with expectations, as large parts of silver are precipitated and only a small portion can be reduced to Ag^0.

Pure silver NPs are the exception here, as only a small portion of the silver is precipitated as AgOH, leaving the majority of the silver reducable. As the resulting Ag^0 concentration is higher than for the bimetallic cases by a factor of 40–50, we plot the concentration of Ag^0 for the case of pure Ag on a second y-axis. Further, it is evident that depending on the precursor ratio of Ag and Au, the peak concentrations for Ag^0 and Au^0 are higher or lower with higher gold precursor ratios leading to higher Au^0 and lower Ag^0 peak concentrations and vice versa. Further, the maximum concentration of Au^0 is reached later in the process the lower the gold precursor is. This can be explained by the lower concentration of gold ions in solution leading to a slower reaction rate to Au^0 and thus a later peak concentration. Lastly, the concentration of AgCl is the highest for a high silver precursor ratio. Interestingly, for the formation of AgAu ANPs with a molar gold content of 50 %, AgCl is present for longer than in the case of the other alloy compositions. This correlates with a slower reaction kinetic (see Fig. 4d and Fig. 8a), showing that redissolving of AgCl is the rate determining step in the process.

4. Conclusion

We propose a formation mechanism of AgAu bimetallic alloy NPs produced via liquid-phase chemical co-reduction, which was unraveled utilizing a variety of advanced characterization techniques, including STEM-EDXS, AUC, and in-line UV–Vis-spectroscopy. Alloy NPs were produced via a green room-temperature one-pot synthesis using dextran as the reducing agent and the stabilizer. The formation proceeds as a six-step process, starting with the precipitation of solid AgCl, followed by the reduction of remaining silver and gold precursors, the nucleation of highly gold rich nuclei, the subsequent growth of a silver-rich shell, the simultaneous redissolving of AgCl into the synthesis mixture, and finally the intraparticulate reorganization of silver and gold atoms to a fully alloyed NP. While these steps can be described as subsequent, they occur partly in parallel. The formation was modelled via a two-dimensional population balance model, which yields a quantitative and predictive description of the process, effectively bridging the property-process relationship for the given particle system.

Our model is not limited to the synthesis of bimetallic ANPs but is based on a widely applicable, general approach. In principle, any formation process, which can be traced back to a (series of) reaction step(s), nucleation, and growth, can be described by the presented model. Unknown or hardly accessible rate and material constants are determined by calibration of the model against measurable data such as size distributions and overall optical properties. Scale-up and process control is now possible based on the revealed formation mechanism and the quantitative formation kinetics.

CRediT authorship contribution statement

N.E. Traoré: Conceptualization, Data curation, Formal analysis, Investigation, Methodology, Visualization, Writing – original draft, Writing – review & editing. **T. Schikarski:** Writing – original draft, Validation, Investigation, Formal analysis. **A. Körner:** Writing – original draft, Investigation, Formal analysis. **P. Cardenas Lopez:** Writing – original draft, Investigation, Formal analysis. **L. Hartmann:** Investigation, Formal analysis. **B. Fritsch:** Formal analysis, Writing – original draft. **J. Walter:** Formal analysis, Resources, Supervision, Validation, Writing – review & editing. **A. Hutzler:** Formal analysis, Investigation, Resources, Supervision, Writing – review & editing. **L. Pflug:** Conceptualization, Formal analysis, Investigation, Methodology, Resources, Supervision, Validation, Writing – original draft, Writing – review & editing. **W. Peukert:** Funding acquisition, Resources, Supervision, Validation, Writing – review & editing.

Declaration of competing interest

The authors declare that they have no known competing financial interests or personal relationships that could have appeared to influence the work reported in this paper.

Data availability

Data for this paper, including all data included in the figures are available at Zenodo.org at https://doi.org/10.5281/zenodo.10204534.

Acknowledgements

We gratefully acknowledge the funding by the Deutsche Forschungsgemeinschaft (DFG, German Research Foundation) – Project-ID 416229255 – SFB 1411. In addition, W.P. and J.W. acknowledge the funding for the Optima AUC by DFG project INST 90-1123-1 FUGG.

Further, we would like to acknowledge Patricia Schmul, Hadi Soltanmoradi, and Sandra Wittpahl for their experimental work and the intensive discussions.

Appendix A. Supplementary data

Supplementary data to this article can be found online at https://doi.org/10.1016/j.cej.2024.149429.

References

[1] S. Thatai, P. Khurana, S. Prasad, D. Kumar, A new way in nanosensors: Gold nanorods for sensing of Fe(III) ions in aqueous media, Microchem. J. 113 (2014) 77–82, https://doi.org/10.1016/j.microc.2013.11.004.

[2] J. Li, L. Yang, Y. Ruan, S. Chu, H. Wang, Z. Li, C. Jiang, B. Liu, L. Yang, Z. Zhang, Dual-Mode Optical Nanosensor Based on Gold Nanoparticles and Carbon Dots for Visible Detection of As(III) in Water, ACS Appl. Nano Mater. 3 (2020) 8224–8231, https://doi.org/10.1021/acsanm.0c01647.

[3] M. Jawad, S. Ali, A. Waseem, F. Rabbani, B.A.Z. Amin, M. Bilal, A.J. Shaikh, Plasmonic effects and size relation of gold-platinum alloy nanoparticles, Advances in Nano Research 7 (2019) 169.

[4] D. Kim, S. Park, J.H. Lee, Y.Y. Jeong, S. Jon, Antibiofouling polymer-coated gold nanoparticles as a contrast agent for in vivo X-ray computed tomography imaging, J. Am. Chem. Soc. 129 (2007) 7661–7665, https://doi.org/10.1021/ja071471p.

[5] Q.-Y. Cai, S.H. Kim, K.S. Choi, S.Y. Kim, S.J. Byun, K.W. Kim, S.H. Park, S.K. Juhng, K.-H. Yoon, Colloidal gold nanoparticles as a blood-pool contrast agent for X-ray computed tomography in mice, Invest. Radiol. 42 (2007) 797–806, https://doi.org/10.1097/RLI.0b013e31811ecdcd.

[6] L.E. Cole, R.D. Ross, J. Tilley, T. Vargo-Gogola, R.K. Roeder, Gold nanoparticles as contrast agents in x-ray imaging and computed tomography, Nanomedicine (Lond.) 10 (2015) 321–341, https://doi.org/10.2217/nnm.14.171.

[7] W. Peukert, D. Segets, L. Pflug, G. Leugering, Unified Design Strategies for Particulate Products, in: Mesoscale Modeling in Chemical Engineering Part I, Elsevier, 2015, pp. 1–81.

[8] J. Polte, X. Tuaev, M. Wuithschick, A. Fischer, A.F. Thuenemann, K. Rademann, R. Kraehnert, F. Emmerling, Formation mechanism of colloidal silver nanoparticles: analogies and differences to the growth of gold nanoparticles, ACS Nano 6 (2012) 5791–5802, https://doi.org/10.1021/nn301724z.

[9] J. Polte, R. Erler, A.F. Thünemann, S. Sokolov, T.T. Ahner, K. Rademann, F. Emmerling, R. Kraehnert, Nucleation and growth of gold nanoparticles studied via in situ small angle X-ray scattering at millisecond time resolution, ACS Nano 4 (2010) 1076–1082, https://doi.org/10.1021/nn901499c.

[10] J. Polte, T.T. Ahner, F. Delissen, S. Sokolov, F. Emmerling, A.F. Thünemann, R. Kraehnert, Mechanism of gold nanoparticle formation in the classical citrate synthesis method derived from coupled in situ XANES and SAXS evaluation, J. Am. Chem. Soc. 132 (2010) 1296–1301, https://doi.org/10.1021/ja906506j.

[11] M. Wuithschick, A. Birnbaum, S. Witte, M. Sztucki, U. Vainio, N. Pinna, K. Rademann, F. Emmerling, R. Kraehnert, J. Polte, Turkevich in New Robes: Key Questions Answered for the Most Common Gold Nanoparticle Synthesis, ACS Nano 9 (2015) 7052–7071, https://doi.org/10.1021/acsnano.5b01579.

[12] X. Wu, C. Lu, Z. Zhou, G. Yuan, R. Xiong, X. Zhang, Green synthesis and formation mechanism of cellulose nanocrystal-supported gold nanoparticles with enhanced catalytic performance, Environ. Sci.: Nano 1 (2014) 71, https://doi.org/10.1039/c3en00066d.

[13] M. Harada, S. Kizaki, Formation Mechanism of Gold Nanoparticles Synthesized by Photoreduction in Aqueous Ethanol Solutions of Polymers Using In Situ Quick Scanning X-ray Absorption Fine Structure and Small-Angle X-ray Scattering, Cryst. Growth Des. 16 (2016) 1200–1212, https://doi.org/10.1021/acs.cgd.5b01168.

[14] D. Rioux, M. Meunier, Seeded Growth Synthesis of Composition and Size-Controlled Gold-Silver Alloy Nanoparticles, J. Phys. Chem. C 119 (2015) 13160–13168, https://doi.org/10.1021/acs.jpcc.5b02728.

[15] A.J. Shaikh, M. Batool, M.A. Yameen, A. Waseem, Plasmonic effects, size and biological activity relationship of Au-Ag alloy nanoparticles, Journal of, Nano Res. 54 (2018) 98–111.

[16] N.E. Traoré, M.J. Uttinger, P. Cardenas Lopez, D. Drobek, L. Gromotka, J. Schmidt, J. Walter, B. Apeleo Zubiri, E. Spiecker, W. Peukert, Green room temperature synthesis of silver-gold alloy nanoparticles, Nanoscale Advances 5 (2023) 1450–1464, https://doi.org/10.1039/d2na00793b.

[17] S. Link, Z.L. Wang, M.A. El-Sayed, Alloy Formation of Gold−Silver Nanoparticles and the Dependence of the Plasmon Absorption on Their Composition, J. Phys. Chem. B 103 (1999) 3529–3533, https://doi.org/10.1021/jp990387w.

[18] J.E.S. van der Hoeven, T.A.J. Welling, T.A.G. Silva, J.E. van den Reijen, C. La Fontaine, X. Carrier, C. Louis, A. van Blaaderen, P.E. de Jongh, In Situ Observation of Atomic Redistribution in Alloying Gold-Silver Nanorods, ACS Nano 12 (2018) 8467–8476, https://doi.org/10.1021/acsnano.8b03978.

[19] X. Huang, X. Wang, X. Wang, X. Wang, M. Tan, W. Ding, X. Lu, P123-stabilized Au–Ag alloy nanoparticles for kinetics of aerobic oxidation of benzyl alcohol in aqueous solution, J. Catal. 301 (2013) 217–226, https://doi.org/10.1016/j.jcat.2013.02.011.

[20] H.K. Daima, P.R. Selvakannan, Z. Homan, S.K. Bhargava, V. Bansal, International Conference on Nanoscience, Technology and Societal Implications (NSTSI): 8–10 Dec 2011, Bhubaneswar, India, IEEE, Piscataway, NJ, 2011, p. 2011.

[21] A. Arvinte, I.-A. Crudu, F. Doroftei, D. Timpu, M. Pinteala, Electrochemical codeposition of silver-gold nanoparticles on CNT-based electrode and their performance in electrocatalysis of dopamine, J. Electroanal. Chem. 829 (2018) 184–193, https://doi.org/10.1016/j.jelechem.2018.10.017.

[22] Y.-H. Chen, C.-S. Yeh, A new approach for the formation of alloy nanoparticles: laser synthesis of gold–silver alloy from gold–silver colloidal mixtures, Chem. Commun. (2001) 371–372, https://doi.org/10.1039/b009854j.

[23] I. Lee, S.W. Han, K. Kim, Production of Au-Ag alloy nanoparticles by laser ablation of bulk alloys, Chem. Commun. (Camb) (2001) 1782–1783, https://doi.org/10.1039/b105437f.

[24] G.A. Sotiriou, S.E. Pratsinis, Antibacterial activity of nanosilver ions and particles, Environ. Sci. Tech. 44 (2010) 5649–5654, https://doi.org/10.1021/es101072s.

[25] M.P. Mallin, C.J. Murphy, Solution-Phase Synthesis of Sub-10 nm Au−Ag Alloy Nanoparticles, Nano Lett. 2 (2002) 1235–1237, https://doi.org/10.1021/nl025774n.

[26] C.M. Nguyen, L.M. Frias Batista, M.G. John, C.J. Rodrigues, K.M. Tibbetts, Mechanism of Gold-Silver Alloy Nanoparticle Formation by Laser Coreduction of Gold and Silver Ions in Solution, J. Phys. Chem. B 125 (2021) 907–917, https://doi.org/10.1021/acs.jpcb.0c10096.

[27] P.R.A.F. Garcia, O. Prymak, V. Grasmik, K. Pappert, W. Wlysses, L. Otubo, M. Epple, C.L.P. Oliveira, An in situ SAXS investigation of the formation of silver nanoparticles and bimetallic silver-gold nanoparticles in controlled wet-chemical reduction synthesis, Nanoscale, Advances 2 (2020) 225–238, https://doi.org/10.1039/c9na00569b.

[28] N. Blommaerts, H. Vanrompay, S. Nuti, S. Lenaerts, S. Bals, S.W. Verbruggen, Unraveling Structural Information of Turkevich Synthesized Plasmonic Gold-Silver Bimetallic Nanoparticles, Small 15 (2019) e1902791.

[29] T. Schikarski, M. Avila, W. Peukert, En route towards a comprehensive dimensionless representation of precipitation processes, Chem. Eng. J. 428 (2022) 131984, https://doi.org/10.1016/j.cej.2021.131984.

[30] Z. Wang, N.E. Traoré, T. Schikarski, L.M. Stiegler, D. Drobek, B.A. Zubiri, E. Spiecker, J. Walter, W. Peukert, L. Pflug, D. Segets, Population balance modeling of InP quantum dots: Experimentally enabled global optimization to identify unknown material parameters, Chem. Eng. Sci. 281 (2023) 119062, https://doi.org/10.1016/j.ces.2023.119062.

[31] T. Schikarski, M. Avila, H. Trzenschiok, A. Güldenpfennig, W. Peukert, Quantitative modeling of precipitation processes, Chem. Eng. J. 444 (2022) 136195.

[32] A. Desai, J. Krynitsky, T.J. Pohida, H. Zhao, P. Schuck, 3D-Printing for Analytical Ultracentrifugation, PLoS One 11 (2016) e0155201.

[33] P. Schuck, Size-distribution analysis of macromolecules by sedimentation velocity ultracentrifugation and lamm equation modeling, Biophys. J . 78 (2000) 1606–1619.

[34] J.-P. Schäfer, Implementierung und Anwendung analytischer und numerischer Verfahren zur Lösung der Maxwellgleichungen für die Untersuchung der Lichtausbreitung in biologischem Gewebe, Univ., Diss, Ulm, 2011.

[35] Wiscombe, W. J, NCAR/TN-140+STR Mie Scattering Calculations: Advances in Technique and Fast, Vector-Speed Computer Codes.

[36] C.F. Bohren, D.R. Huffman, Absorption and Scattering of Light by Small Particles, Wiley, 1998.

[37] D. Rioux, S. Vallières, S. Besner, P. Muñoz, E. Mazur, M. Meunier, An Analytic Model for the Dielectric Function of Au, Ag, and their Alloys, Advanced, Opt. Mater. 2 (2014) 176–182, https://doi.org/10.1002/adom.201300457.

[38] J.P. Toennies, U. Gonser, R.M. Osgood, M.B. Panish, H. Sakaki, H.K.V. Lotsch, U. Kreibig, M. Vollmer, Optical Properties of Metal Clusters, Springer, Berlin Heidelberg, Berlin, Heidelberg, 1995.

[39] L.J. Mendoza Herrera, D.M. Arboleda, D.C. Schinca, L.B. Scaffardi, Determination of plasma frequency, damping constant, and size distribution from the complex dielectric function of noble metal nanoparticles, J. Appl. Phys. 116 (2014) 233105, https://doi.org/10.1063/1.4904349.

[40] A. Derkachova, K. Kolwas, I. Demchenko, Dielectric Function for Gold in Plasmonics Applications: Size Dependence of Plasmon Resonance Frequencies and Damping Rates for Nanospheres, Plasmonics 11 (2016) 941–951, https://doi.org/10.1007/s11468-015-0128-7.

[41] J.M.J. Santillán, F.A. Videla, M.B. van Fernández Raap, D. Muraca, L.B. Scaffardi, D.C. Schinca, Influence of size-corrected bound-electron contribution on nanometric silver dielectric function. Sizing through optical extinction spectroscopy, J. Phys. D Appl. Phys. 46 (2013) 435301, https://doi.org/10.1088/0022-3727/46/43/435301.

[42] M.A. Hartig, N. Jacobsen, W. Peukert, Multi-component and multi-phase population balance model: The case of Georgeite formation as methanol catalyst precursor phase, Chem. Eng. Sci. 109 (2014) 158–170, https://doi.org/10.1016/j.ces.2014.01.026.

[43] M. Haderlein, A. Güldenpfennig, D. Segets, W. Peukert, A widely applicable tool for modeling precipitation processes, Comput. Chem. Eng. 98 (2017) 197–208, https://doi.org/10.1016/j.compchemeng.2016.12.007.

[44] I. Ojea-Jiménez, J.M. Campanera, Molecular Modeling of the Reduction Mechanism in the Citrate-Mediated Synthesis of Gold Nanoparticles, J. Phys. Chem. C 116 (2012) 23682–23691, https://doi.org/10.1021/jp305830p.

[45] A.S. Myerson, D. Erdemir, A.Y. Lee (Eds.), Handbook of Industrial Crystallization, Cambridge University Press, Cambridge, 2019.

[46] Konrad Bates Krauskopf, The Solubility of Gold.

[47] C.V. Thompson, Solid-State Dewetting of Thin Films, Annu. Rev. Mat. Res. 42 (2012) 399–434, https://doi.org/10.1146/annurev-matsci-070511-155048.

[48] J. Ye, C.V. Thompson, Regular pattern formation through the retraction and pinch-off of edges during solid-state dewetting of patterned single crystal films, Phys. Rev. B 82 (2010), https://doi.org/10.1103/PhysRevB.82.193408.

[49] K. Aliyah, J. Lyu, C. Goldmann, T. Bizien, C. Hamon, D. Alloyeau, D. Constantin, Real-Time In Situ Observations Reveal a Double Role for Ascorbic Acid in the Anisotropic Growth of Silver on Gold, J. Phys. Chem. Lett. 11 (2020) 2830–2837, https://doi.org/10.1021/acs.jpclett.0c00121.

[50] S. Gómez-Graña, B. Goris, T. Altantzis, C. Fernández-López, E. Carbó-Argibay, A. Guerrero-Martínez, N. Almora-Barrios, N. López, I. Pastoriza-Santos, J. Pérez-Juste, S. Bals, G. van Tendeloo, L.M. Liz-Marzán, Au@Ag Nanoparticles: Halides Stabilize 100 Facets, J. Phys. Chem. Lett. 4 (2013) 2209–2216, https://doi.org/10.1021/jz401269w.

[51] D.R. Handwerk, P.D. Shipman, C.B. Whitehead, S. Özkar, R.G. Finke, Particle Size Distributions via Mechanism-Enabled Population Balance Modeling, J. Phys. Chem. C 124 (2020) 4852–4880, https://doi.org/10.1021/acs.jpcc.9b11239.

[52] Y.A. Wu, L. Li, Z. Li, A. Kinaci, M.K.Y. Chan, Y. Sun, J.R. Guest, I. McNulty, T. Rajh, Y. Liu, Visualizing Redox Dynamics of a Single Ag/AgCl Heterogeneous Nanocatalyst at Atomic Resolution, ACS Nano 10 (2016) 3738–3746, https://doi.org/10.1021/acsnano.6b00355.

[53] S. Ristig, O. Prymak, K. Loza, M. Gocyla, W. Meyer-Zaika, M. Heggen, D. Raabe, M. Epple, Nanostructure of wet-chemically prepared, polymer-stabilized silver-gold nanoalloys (6 nm) over the entire composition range, J. Mater. Chem. B 3 (2015) 4654–4662, https://doi.org/10.1039/c5tb00644a.

[54] Z.Y. Li, J.P. Wilcoxon, F. Yin, Y. Chen, R.E. Palmer, R.L. Johnston, Structures and optical properties of 4-5 nm bimetallic AgAu nanoparticles, Faraday Discuss. 138 (2008) 363-73; discussion 421-34. https://doi.org/10.1039/b708958a.

[55] E. Clementi, D.L. Raimondi, W.P. Reinhardt, Atomic Screening Constants from SCF Functions. II. Atoms with 37 to 86 Electrons, J. Chem. Phys. 47 (1967) 1300–1307, https://doi.org/10.1063/1.1712084.

[56] T. Guo, Y. Tan, Formation of one-dimensional Ag-Au solid solution colloids with Au nanorods as seeds, their alloying mechanisms, and surface plasmon resonances, Nanoscale 5 (2013) 561–569, https://doi.org/10.1039/c2nr32862c.

[57] W. Haiss, N.T.K. Thanh, J. Aveyard, D.G. Fernig, Determination of size and concentration of gold nanoparticles from UV-vis spectra, Anal. Chem. 79 (2007) 4215–4221, https://doi.org/10.1021/ac0702084.

[58] P. Cardenas Lopez, M.J. Uttinger, N.E. Traoré, H.A. Khan, D. Drobek, B. Apeleo Zubiri, E. Spiecker, L. Pflug, W. Peukert, J. Walter, Multidimensional

characterization of noble metal alloy nanoparticles by multiwavelength analytical ultracentrifugation, Nanoscale (2022), https://doi.org/10.1039/D2NR02633C.
[59] T. Kunz, E.J. Lee, V. Schiwek, T. Seewald, F.J. Methner, Glucose—A reducing sugar? Reducing properties of sugars in beverages and food, Brew. Sci 64 (2011) 61–67.
[60] S. Waffenschmidt, L. Jaenicke, Assay of reducing sugars in the nanomole range with 2, 2′-bicinchoninate, Anal. Biochem. 165 (1987) 337–340.
[61] J.F. Gomes, A.C. Garcia, E.B. Ferreira, C. Pires, V.L. Oliveira, G. Tremiliosi-Filho, L. H.S. Gasparotto, New insights into the formation mechanism of Ag, Au and AgAu nanoparticles in aqueous alkaline media: alkoxides from alcohols, aldehydes and ketones as universal reducing agents, PCCP 17 (2015) 21683–21693, https://doi.org/10.1039/c5cp02155c.
[62] C. Han, L. Ge, C. Chen, Y. Li, Z. Zhao, X. Xiao, Z. Li, J. Zhang, Site-selected synthesis of novel Ag@AgCl nanoframes with efficient visible light induced photocatalytic activity, J. Mater. Chem. A 2 (2014) 12594–12600, https://doi.org/10.1039/C4TA01941E.
[63] J.-F. Guo, B. Ma, A. Yin, K. Fan, W.-L. Dai, Highly stable and efficient Ag/AgCl@TiO2 photocatalyst: preparation, characterization, and application in the treatment of aqueous hazardous pollutants, J. Hazard. Mater. 211–212 (2012) 77–82, https://doi.org/10.1016/j.jhazmat.2011.11.082.
[64] R. Dong, B. Tian, C. Zeng, T. Li, T. Wang, J. Zhang, Ecofriendly Synthesis and Photocatalytic Activity of Uniform Cubic Ag@AgCl Plasmonic Photocatalyst, J. Phys. Chem. C 117 (2013) 213–220, https://doi.org/10.1021/jp311970k.
[65] M. Biegel, T. Schikarski, P. Cardenas Lopez, L. Gromotka, C. Lübbert, A. Völkl, C. Damm, J. Walter, W. Peukert, Efficient quenching sheds light on early stages of gold nanoparticle formation, RSC, Advances 13 (2023) 18001–18013, https://doi.org/10.1039/D3RA02195E.
[66] N.T.K. Thanh, N. Maclean, S. Mahiddine, Mechanisms of nucleation and growth of nanoparticles in solution, Chem. Rev. 114 (2014) 7610–7630, https://doi.org/10.1021/cr400544s.
[67] X. Ma, Y. Dai, L. Yu, Z. Lou, B. Huang, M.-H. Whangbo, Electron-Hole Pair Generation of the Visible-Light Plasmonic Photocatalyst Ag@AgCl: Enhanced Optical Transitions Involving Midgap Defect States of AgCl, J. Phys. Chem. C 118 (2014) 12133–12140, https://doi.org/10.1021/jp5023604.
[68] A. Hutzler, T. Schmutzler, M.P.M. Jank, R. Branscheid, T. Unruh, E. Spiecker, L. Frey, Unravelling the Mechanisms of Gold-Silver Core-Shell Nanostructure Formation by in Situ TEM Using an Advanced Liquid Cell Design, Nano Lett. 18 (2018) 7222–7229, https://doi.org/10.1021/acs.nanolett.8b03388.
[69] A. Muneer, T. Schikarski, L. Pflug, Exact Method of Moments for multi-dimensional population balance equations, 2023.
[70] A. Mersmann, K. Bartosch, B. Braun, A. Eble, C. Heyer, Möglichkeiten einer vorhersagenden Abschätzung der Kristallisationskinetik, Chem.-Ing.-Tech. 72 (2000) 17–30, https://doi.org/10.1002/1522-2640(200001)72:1/2<17:AID-CITE17>3.0.CO;2-T.
[71] A. Keimer, L. Pflug, M. Spinola, Existence, uniqueness and regularity of multi-dimensional nonlocal balance laws with damping, J. Math. Anal. Appl. 466 (2018) 18–55, https://doi.org/10.1016/j.jmaa.2018.05.013.
[72] L. Pflug, T. Schikarski, A. Keimer, W. Peukert, M. Stingl, eMoM: Exact method of moments—Nucleation and size dependent growth of nanoparticles, Comput. Chem. Eng. 136 (2020) 106775, https://doi.org/10.1016/j.compchemeng.2020.106775.
[73] W.H. Press, S.A. Teukolsky, W.T. Vetterling, B.P. Flannery, M. Metcalf, Numerical Recipes in 1 (1992) 9.
[74] A. Mersmann, Calculation of interfacial tensions, J. Cryst. Growth 102 (1990) 841–847.
[75] A. Mersmann, Crystallization Technology Handbook, 2nd edition, rev. and expanded.,, Marcel Dekker, New York, 2001.
[76] K.-S. Chou, Y.-C. Lu, H.-H. Lee, Effect of alkaline ion on the mechanism and kinetics of chemical reduction of silver, Mater. Chem. Phys. 94 (2005) 429–433, https://doi.org/10.1016/j.matchemphys.2005.05.029.
[77] S.P. Mushran, M.C. Agrawal, R.M. Mehrotra, R. Sanehi, Kinetics and mechanism of reduction of silver(I) by ascorbic acid, J. Chem. Soc. Dalton Trans. (1974) 1460, https://doi.org/10.1039/DT9740001460.
[78] L.M. Liz-Marzán, I. Lado-Touriño, Reduction and stabilization of silver nanoparticles in ethanol by nonionic surfactants, Langmuir 12 (1996) 3585–3589.
[79] M. Luty-Błocho, M. Wojnicki, K. Fitzner, Gold Nanoparticles Formation via Au(III) Complex Ions Reduction with l -Ascorbic Acid, Int. J. Chem. Kinet. 49 (2017) 789–797, https://doi.org/10.1002/kin.21115.
[80] I. Pastoriza-Santos, L.M. Liz-Marzán, Formation and Stabilization of Silver Nanoparticles through Reduction by N N -Dimethylformamide, Langmuir 15 (1999) 948–951, https://doi.org/10.1021/la980984u.
[81] A. Kundu, R.K. Layek, A. Kuila, A.K. Nandi, Highly fluorescent graphene oxide-poly (vinyl alcohol) hybrid: an effective material for specific Au3+ ion sensors, ACS Appl. Mater. Interfaces 4 (2012) 5576–5582, https://doi.org/10.1021/am301467z.
[82] N.L. Pacioni, C.D. Borsarelli, V. Rey, A.V. Veglia, Synthetic Routes for the Preparation of Silver Nanoparticles, in: E.I. Alarcon, M. Griffith, K.I. Udekwu (Eds.), Silver Nanoparticle Applications, Springer International Publishing, Cham, 2015, pp. 13–46.
[83] Quantitative Chemical Analysis, Spektrum Akademischer Verlag Gmbh, 2013.
[84] Y. Bi, J. Ye, In situ oxidation synthesis of Ag/AgCl core-shell nanowires and their photocatalytic properties, Chem. Commun. (2009) 6551–6553, https://doi.org/10.1039/B913725D.
[85] A. Zaleska-Medynska, M. Marchelek, M. Diak, E. Grabowska, Noble metal-based bimetallic nanoparticles: the effect of the structure on the optical, catalytic and photocatalytic properties, Adv. Colloid Interface Sci. 229 (2016) 80–107, https://doi.org/10.1016/j.cis.2015.12.008.
[86] S.K. Sahoo, M.R. Hormozi-Nezhad, Gold and silver nanoparticles: Synthesis and applications, Elsevier, Amsterdam, Netherlands, Oxford, United Kingdom, Cambridge MA, 2023.